Delivery of anthropogenic bioavailable iron from mineral dust and combustion aerosols to the ocean

Akinori Ito[1*] and Zongbo Shi[2]

[1]Yokohama Institute for Earth Sciences, JAMSTEC, Yokohama, Kanagawa, Japan

[2]School of Geography, Earth and Environmental Sciences, University of Birmingham, Birmingham, U.K. *e-mail: akinorii@jamstec.go.jp

Running Title: **Anthropogenic bioavailable Fe deposition**

Keywords:

Atmospheric deposition; soluble iron; organic aerosol; mineral dust; environmental changes

Abstract. Atmospheric deposition of anthropogenic soluble iron (Fe) to the ocean has been suggested to modulate primary ocean productivity and thus indirectly affect the climate. A key process contributing to anthropogenic sources of soluble Fe is associated with air pollution, which acidifies Fe-containing mineral aerosols during their transport and leads to Fe transformation from insoluble to soluble forms. However, there is large uncertainty in our estimate of this anthropogenic soluble Fe. In this study, for the first time, we interactively combined laboratory kinetic experiments with global aerosol modeling to more accurately quantify anthropogenic soluble Fe due to air pollution. Firstly, we determined Fe dissolution kinetics of African dust samples at acidic pH values with and without ionic species commonly found in aerosol water (i.e., sulfate and oxalate). Then, we constructed a new empirical scheme for Fe release from mineral dust due to inorganic and organic anions in aerosol water, by using acidity as a master variable. We implemented this new scheme and applied an updated mineralogical emission database in a global atmospheric chemistry transport model to estimate the atmospheric concentration and deposition flux of soluble Fe under preindustrial and modern conditions. Our improved model successfully captured the inverse relationship of Fe solubility and total Fe loading measured over the North Atlantic Ocean (i.e., 1–2 orders of magnitude lower Fe solubility in North African- than combustion-influenced aerosols). The model results show a positive relationship between Fe solubility and water soluble organic carbon (WSOC)/Fe molar ratio, which is consistent with previous field measurements. We estimated that deposition of soluble Fe to the ocean increased from 0.05–0.07 Tg Fe yr^{-1} in preindustrial era to 0.11–0.12 Tg Fe yr^{-1} in present days, due to air pollution. Over the High Nitrate Low Chlorophyll (HNLC) regions of the ocean, the modeled Fe solubility remains low for mineral dust (<1%) in a base simulation but is substantially enhanced in a sensitivity simulation, which permits the Fe dissolution for mineral aerosols in the presence of excess oxalate under low acidity during daytime. Our model results suggest that human activities contribute to about half of the soluble Fe supply to a significant portion of the oceans in the Northern Hemisphere, while their contribution to oceans in high latitudes remains uncertain due to limited understanding of Fe source and its dissolution under pristine conditions.

1 Introduction

Changes in supply of nutrients such as bioavailable iron (Fe) from the atmosphere to the ocean have altered oceanic carbon uptake, but significant uncertainties remain on the magnitude of this effect (Ciais et al., 2013). Thus improved quantification of atmospheric delivery of bioavailable Fe is essential to quantify the long-term carbon sink (Jickells et al. 2005). The present study focuses on "potentially" bioavailable Fe, which includes colloidal materials and aqueous species (often operationally defined as soluble Fe). The response of the aerosol Fe solubility (i.e., soluble Fe / total Fe) to air pollution is a key uncertainty in our understanding of the biogeochemical cycle of Fe, marine ecosystem, and climate (Mahowald et al., 2009; Shi et al. 2012; Hajima et al., 2014).

Atmospheric processing of mineral dust has been hypothesized to be an important source of soluble Fe to the oceans because of acidic condition in aerosol water (Zhuang et al. 1992; Meskhidze et al., 2003). Previous chemical transport models used mineral dissolution rates and stoichiometric numbers of Fe in minerals to estimate Fe release rates from mineral aerosols (Meskhidze et al., 2005; Solmon et al., 2009; Ito and Feng, 2010; Ito, 2012). Laboratory studies for mineral dust have demonstrated that the Fe release rates used in previous global models were much slower than the measurements during a typical aerosol lifetime of 2–7 days (Mackie et al., 2005; Shi et al., 2011). The initial period of enhanced concentration of elements, which are incongruently dissolved in solution from phyllosilicate minerals, is well known in laboratory works (e.g., Malmström and Banwart, 1997; Brandt et al., 2003). Much slower quasi-steady state dissolution rates after 10–14 days are typically observed for aluminosilicate minerals in acid solutions (Amram and Ganor, 2005; Lowson et al., 2005; Golubev et al., 2006; Rozalén et al., 2008; Bibi et al., 2011). Recent atmospheric chemical transport models have adopted the initial period of enhanced Fe release rate for the proton-promoted dissolution (Ito and Xu, 2014; Myriokefalitakis et al., 2015). In previous studies, which implemented the proton-promoted Fe dissolution with no organic ligand, the Fe dissolution was significantly suppressed due to the dust alkalinity, particularly in the Southern Hemisphere (Meskhidze et al., 2005; Ito and Feng, 2010; Johnson et al., 2010; Ito and Xu, 2014). Currently, ferric sulfate is treated as water-soluble Fe in oil combustion aerosols at emission (Ito, 2013, 2015; Myriokefalitakis et al., 2015; Wang et al., 2015).

Previous laboratory studies suggest that different acid types and photochemical reactions affect proton-promoted Fe dissolution rates of mineral dust, in addition to the types of Fe species associated with mineral source materials (Cwiertny et al., 2008; Fu et al., 2010; Rubasinghege et al., 2010). However, all previous laboratory experiments were conducted in absence of ammonium salt, such as sulfate, which are ubiquitous in aerosol water. Some of anions in aerosol water are known to be effective inorganic ligands, which form the complexes with Fe in solution (Cornell and Schwertmann, 2003). In batch experiments, the mineral dissolution rate at high dust/liquid ratio can be influenced by different ability of these anions to form soluble complexes with metals (Hamer et al., 2003). Thus the effect of decrease of the activity of Fe^{3+} on the Fe dissolution rates via the formation of aqueous complexes needs to be assessed in laboratory experiments to constrain the degree of suppression used in models.

Recently, global atmospheric transport model studies have emphasized the role of oxalate for promoting Fe dissolution from Fe-containing aerosols (Luo and Gao, 2010; Johnson and Meskhidze, 2013; Ito, 2015; Myriokefalitakis et al., 2015) (see the Supplement). Moreover, oxalate-promoted dissolution of Fe is suppressed at low concentrations of oxalate near strong Fe sources (Ito, 2015), because excess oxalate is necessary to induce significant Fe dissolution

(Chen and Grassian, 2013). These modeling studies highlighted the importance of oxalate-promoted Fe dissolution for mineral dust over the remote oceans. However, a constant oxalate-promoted dissolution rate with time for mineral dust has been prescribed in previous models regardless of different dissolution behaviors in different Fe types, due to a lack of experimental data for oxalate-promoted Fe dissolution kinetics.

Here, we conducted a series of laboratory experiments to examine how inorganic and organic ligands in solution (i.e., sulfate and oxalate) affect Fe dissolution rates in mineral dust. The experimental data were then used to derive a new Fe release scheme, which is implemented in a global chemical transport model to quantify the effect of atmospheric processing of mineral aerosols on Fe mobilization. This study incorporates the proton- and oxalate-promoted Fe dissolution schemes for the mineral aerosols in our model (Ito, 2015). We also examine quasi-photo-reductive dissolution scheme for mineral aerosols in a sensitivity simulation. Determination of Fe dissolution for different types of Fe requires three key parameters of Fe release rate, degree of suppression, and Fe content. We implement three-stage kinetic process for the Fe dissolution scheme to dust aerosols. We use the updated version of the mineralogical database for Fe content in soils (Journet et al., 2014). To assess model assumptions for Fe dissolution, the calculated Fe solubility is evaluated against field observations in relation to total Fe loading and water soluble organic carbon (WSOC) over the North Atlantic Ocean (Wozniak et al. 2013, 2015). The model estimates “anthropogenic” soluble Fe supply from both dust and combustion sources to the oceans in association with changes in air quality based on the Intergovernmental Panel on Climate Change (IPCC) emission data set. We use the term “anthropogenic” soluble Fe here as primary soluble Fe from oil combustion aerosols and secondary soluble Fe from both dust and combustion aerosols, due to the changes in emissions from fossil fuel use and biofuel combustion between the preindustrial era and the present day (Ito et al., 2014).

2 Laboratory experiments

In this study, we used the same Tibesti dust sample as in Shi et al. (2011). We followed a similar methodology as in Shi et al. (2011). Please see supplementary materials for more details. In order to determine the Fe dissolution kinetics in the dust aerosol water, which contains organic ligands, such as oxalate, and high concentration of inorganic ions, such as sulfate, four sets of time dependent dissolution experiments were performed, as is summarized in Table 1. The experiments include the dissolution of Fe in the Tibesti dust:

(Experiment 1) at a dust/liquid ratio of 1 g L^{-1} in 0.05 and 0.005 mol L^{-1} sulfuric acid solution only (i.e., no $(NH_4)_2SO_4$) (pH = 1.3, ionic strength $I = 0.15$ M; and pH = 2.1, $I = 0.015$ M). The pH values in highly acidic solutions were estimated from molality and activity coefficient, which were calculated using E-AIM III aqueous solution simulator (Wexler and Clegg, 2002).

(Experiment 2) at a dust/liquid ratio of 1 g L^{-1} in 0.05 and 0.0005 mol L^{-1} sulfuric acid solution with 1 mol L^{-1} $(NH_4)_2SO_4$ (pH = 2 and $I = 3.15$ M; and pH = 3.1 and $I = 3.015$ M) only (i.e., no oxalate) and in 0.1 mol L^{-1} HCl solution with 3 mol L^{-1} NH_4Cl (ionic strength $I = 3.2$ mol L^{-1}) (pH = 0.9; note that activity coefficient for H^+ in this solution is higher than 1), and at a dust/liquid ratio of 10 g L^{-1} in 0.05 mol L^{-1} sulfuric acid solution with 1 mol L^{-1} $(NH_4)_2SO_4$ (pH = 2, $I = 3.15$ mol kg^{-1}). The pH values with high ionic strength ($I > 3$ mol L^{-1}) were estimated using E-AIM III thermodynamic model (Wexler and Clegg, 2002).

(Experiment 3) at a dust/liquid ratio of 1 g L^{-1} in 0.05 and 0.0005 mol L^{-1} sulfuric acid solution with both 1 mol L^{-1} $(NH_4)_2SO_4$ and 0.03 mol L^{-1} of oxalate (as sodium oxalate) (pH = 2, I = 3.15 M; and pH = 3.1, I = 3.015 M). The chosen amount of oxalate is based on the molar ratio of oxalate and sulfate in ambient $PM_{2.5}$ samples (Yu et al., 2005).

(Experiment 4) at a dust/liquid ratio of 60 mg L^{-1}, 10 g L^{-1} and 50 g L^{-1} in 0.005 mol L^{-1} sulfuric acid solution (pH 2). The pH was continuously monitored during the experiments at four different dust/liquid ratios (i.e., 60 mg L^{-1}, 1 g L^{-1}, 10 g L^{-1} and 50 g L^{-1}) and once the pH change was more than 0.1 pH unit, acids were added to decrease the pH to 2. This aims to determine how different dust/liquid ratios affect the Fe dissolution kinetics in comparison with experiment (1) (1 g L^{-1}).

3 Model description

This study uses the Integrated Massively Parallel Atmospheric Chemical Transport (IMPACT) model (Rotman et al., 2004; Liu et al., 2005; Feng and Penner, 2007; Ito et al., 2007, 2012, 2014, 2015; Lin et al., 2014; Xu and Penner, 2012; Ito, 2015). The model is driven by assimilated meteorological fields from the Goddard Earth Observation System (GEOS) of the NASA Global Modeling and Assimilation Office (GMAO). Simulations have been performed with a horizontal resolution of 2.0° × 2.5° and 59 vertical layers with a top boundary at 0.01 hPa using meteorological fields for the year 2010 (and 2011 for the comparison with the field measurements).

We run the model with emissions of primary aerosols and precursor gases of secondary aerosols such as sulfate, nitrate, ammonium, and oxalate for the preindustrial era and the present day to disentangle the naturally and anthropogenically-perturbed components (Table 2), as described in Ito et al. (2014). The emission data sets for anthropogenic activities such as fossil fuel use and biofuel combustion are taken from the historical emissions for IPCC Fifth Assessment (AR5) report for the preindustrial era and the present day (Lamarque et al., 2010). The present-day estimates for mineral aerosols from arid and semiarid regions as well as combustion aerosols from biomass burning are used together with anthropogenic emission changes (Ito and Xu, 2014; Ito et al., 2015; Ito, 2015). The same natural emissions of dimethylsulfide (DMS), sulfur dioxide (SO_2), nitrogen oxides (NO_x), volatile organic compounds (VOCs), and ammonia (NH_3) are used for both periods in our simulations, as we use the same meteorological data set. Thus Fe-dissolution due to natural acidity is not included in the "anthropogenic" fraction of soluble Fe, as in Ito and Xu (2014).

Previously, Ito and Xu (2014) used the mineralogical database compiled by Nickovic et al. (2012) and Fe content for hematite (69.9%), illite (4.0%), smectite (11%), kaolinite (0.24%), and feldspars (0.34%) (Journet et al., 2008). Here, the updated global database of mineral composition and Fe content for hematite (69.9%), goethite (62.8%), illite (4.3%), smectite (2.6%), kaolinite (0.23%), chlorite (12.3%), vermiculite (6.71%), and feldspars (0.34%) in clay-sized and silt-sized soils (CASE 1 in Journet et al., 2014) was used to estimate the emissions of Fe and calcite in dust aerosols. The size distribution at emission follows the mass fractions of emitted soil particles in Kok (2011). The mass fluxes of mineral dust at emission are interpolated to represent four model size bins (radius: <0.63, 0.63–1.25, 1.25–2.5, and 2.5–10 μm) with the theoretical expression (Ito et al., 2012). The mineral fractions in clay-sized and silt-sized soils are also distributed in the 4 size bins following the brittle fragmentation theory after Scanza et al. (2015). All the Fe-containing minerals are found in the clay-sized soils, while only three minerals (i.e., goethite, chlorite, and feldspars) are in the silt-sized soils (Journet et al., 2014).

Thus Fe content averaged in the 1–3 size bins (3.6%) is higher than the largest one (2.3%), in contrast to constant Fe content (3.1%) with size in previous version. As a result, global Fe emission from dust (69 Tg yr^{-1}) is slightly smaller than that estimated in the previous version (79 Tg yr^{-1}) (Ito, 2015). The sum of Fe emission in the smaller size from bin 1 to bin 3 in this study (25 Tg yr^{-1}) is larger than that in the previous version (22 Tg yr^{-1}). Consequently, smaller dust particles may transport more Fe to remote regions relative to larger particles.

Mineral dust aging process with the formation of soluble materials in aerosol and cloud water (e.g., sulfate, nitrate, ammonium, and oxalate) is explicitly simulated in the model (Ito and Xu, 2014; Ito, 2015). The values of the pH of the aerosol water used in the calculations of the dissolution rates are estimated for all of the wet aerosols in each size bin, as in Ito and Xu (2014). The aqueous-phase chemical reactions for the formation of oxalate are the same as described by Lin et al. (2014), except for the treatment of the Fe chemistry in aerosol and cloud water as in Ito (2015). Thus Fe(III)-oxalate complex is the major form of Fe in modeled solution. The photolysis of Fe-oxalate complex can contribute to a significant oxalate sink in cloud water influenced by ship emissions (Sorooshian et al., 2013; Wang et al., 2014). On the other hand, a complexation of Fe(II) with stronger organic ligands from fossil fuel combustion may be important for the stability of Fe dissolved in rain water (Kieber et al., 2005; Willey et al., 2015). Here, we focus on the acid mobilization of relatively insoluble Fe in Fe-containing minerals to soluble Fe. Because of the lack of knowledge regarding the specific ligands and formation rates of Fe-organic complexes, Fe chemistry is disabled in cloud and rain water but implemented for Fe-containing wet aerosols in four size bins to obtain good agreement regarding oxalate with the observations over the ocean (see Figure S3 in Ito, 2015). The deposition velocities of soluble Fe depend on the aerosol types and size bins, and follow the aging of the parent aerosols in the atmosphere (Ito and Xu, 2014). Here, we developed a new Fe release scheme in mineral dust (see section 4) to improve the previously used scheme (Ito and Xu, 2014). The new scheme is implemented in the IMPACT model for simulations in section 5.

4. Development of a new Fe dissolution scheme based on new experimental results

In our model, Fe release from aerosols due to chemical processing is calculated based on an online simulation of aqueous-phase chemistry (Ito and Feng, 2010; Ito, 2012; Ito and Xu, 2014; Ito, 2015). Ito and Xu (2014) have developed a Fe dissolution scheme that considers the types of Fe species associated with mineral source materials, mainly based on the measurements by Shi et al. (2011). Following their studies, three Fe pools are characterized by ferrihydrite, nano-sized Fe oxides, and heterogeneous inclusion of nano-Fe grains in aluminosilicates (e.g., illite, smectite, and chlorite). Here we developed a new Fe dissolution scheme, which considers our laboratory experimental datasets regarding: (1) the formation of Fe inorganic and organic complexes in solution and (2) the formation of surface complexes between oxalate and Fe oxides, following Ito (2015) for combustion aerosols.

Figure 1 and Fig. S1 demonstrate the effects of inorganic anions to form soluble complexes with Fe at different dust/liquid ratios on dissolution rates measured in acidic solution. Figure 1 shows that the pH = 2 (0.05M H_2SO_4, 1M $(NH_4)_2SO_4$, red triangles) and pH = 2.1 (0.005M H_2SO_4, green diamonds) cases at 1 g dust L^{-1} have significantly different Fe dissolution rates. The one with high ionic strength (red triangles, Figure 1) has a much higher dissolution rate than predicted by the small difference in the pH values. It is expected that one pH unit can lead to 3–4 times difference in dissolution rates as shown here and by Shi et al. (2011). The presence of complexing ions such as sulfate in this case has the potential to accelerate the dissolution rate by absorption or by complexation with Fe dissolved in solution (Cornell and Schwertmann, 2003). We observed a good agreement of measurements between at 1 g L^{-1} dust in 0.05 mol L^{-1} sulfuric acid solution with 1 mol L^{-1} $(NH_4)_2SO_4$ (pH = 2.0, red triangles) and at 60 mg L^{-1} dust in 0.005 mol L^{-1} sulfuric acid solution without $(NH_4)_2SO_4$ (pH = 2.11, black circles). Thus the solution remains under-saturated with respect to Fe(III), because essentially all aqueous Fe(III) species (> 99%) is complexed with sulfate (i.e., $FeSO_4^+$) in 0.05 mol L^{-1} sulfuric acid solution with 1 mol L^{-1} $(NH_4)_2SO_4$ (pH = 2.0) (Meskhidze et al., 2005; Ito, 2015). The higher dust/liquid ratio at 10 g L^{-1} (blue squares) exhibits lower Fe dissolution rate after the initial period of enhanced Fe release rate, possibly due to the re-adsorption of solution phase Fe onto the particulate phase, as the solution with $(NH_4)_2SO_4$ is under-saturated with respect to Fe(III) (Spokes and Jickells, 1996; Bibi et al., 2011).

Our data indicate that addition of complexing agents (i.e., sulfate in Fig. 1 and chlorite in Fig. S1) accelerated dissolution of Fe minerals by binding Fe released from the surface in solution (Zhang et al., 1985; Xu and Gao, 2008). Almost identical slopes were found at between 1 g dust L^{-1} in 0.05 mol L^{-1} sulfuric acid solution with 1 M $(NH_4)_2SO_4$ (pH = 2.0, red triangles) and 60 mg dust L^{-1} in 0.005 mol L^{-1} sulfuric acid solution without $(NH_4)_2SO_4$ (pH = 2.0, black circles) during a typical aerosol lifetime (Fig. 1). Thus we chose dust/liquid ratios of 1 g dust L^{-1} in sulfuric acid solution with 1 M ammonium sulfate to represent proton-promoted Fe dissolution scheme for mineral dust.

Figure 2 demonstrates the impact of oxalate on Fe dissolution rate (black circles). The addition of 0.03 M $Na_2C_2O_4$ accelerated the dissolution of Fe in 1 g dust L^{-1} solution, 0.05 M H_2SO_4 or 0.005 M H_2SO_4, with 1 M $(NH_4)_2SO_4$. Dissolved Fe concentration was 60% higher at 72 h in the 0.05 M H_2SO_4 and 1 M $(NH_4)_2SO_4$ dust suspensions with oxalate. It was over 100%

higher at 72 h in the 0.005 M H_2SO_4 and 1 M $(NH_4)_2SO_4$) dust suspensions when added oxalate. The higher activity of protons can facilitate the oxalate-promoted dissolution process by protonating the hydroxyl (OH) groups at the surface of hydrous Fe oxides, thereby contributing to increasing the number of positively charged surface sites. This increase promotes ligand adsorption, and weakening of the Fe-O bond, which permits the reaction between oxalate and Fe sites by ligand exchange (Cornell and Schwertman, 2003; Ramos et al., 2014). Although the protonation of the ligands in solution increases at higher activity of protons, the adsorption mechanism of $HC_2O_4^-$ involves the loss of a proton during the ligand-exchange adsorption reaction or during the transfer process from bulk solution to the mineral surface (Yoon et al., 2004). Consequently, the amount of absorbed complex on the mineral surface is higher in solutions at $pH < 7$ when the overall charge at the reactive surface sites is positive, compared to that at lower activity of protons (Zhang et al., 1985; Xu and Gao, 2008; Lanzl et al., 2012; Ramos et al., 2014). The surface biding sites for adsorbed oxalate become saturated at high proton and high oxalate concentrations, and thus oxalate-promoted dissolution rates are almost independent of pH for mineral dust (Yoon et al., 2004; Cama and Ganor, 2006; Lanzl et al., 2012).

Experimental data in Fig. 3 demonstrate that the Fe release under higher dust/solution ratios is suppressed when the solution becomes super-saturated with respect to Fe(III), as observed by the decrease in the rate (black circles). At low dust/liquid ratio of 60 mg L^{-1} at pH 2.1 (H^+ concentration of 0.01 mol L^{-1}), Fe dissolution continued even after 800 hours. The rate of Fe dissolution decreased substantially with increasing dust/liquid ratio. At a dust/liquid ratio of 50 g L^{-1}, Fe dissolution stopped at 180 h and only 1.2% (10 µmol g^{-1}) of the total Fe was dissolved, half of which released in the first hour. The calculated thermodynamic solubility of this Fe pool at pH 2 is –3.34 (mol L^{-1} on a log scale). This is comparable to the previously measured solubility of nanogoethite, which is –3.6 (mol L^{-1}) at pH = 2 (see Fig.7 in Shi et al. 2011). Thus this Fe pool likely includes ferrihydrite and reactive nano-Fe oxides aggregated on the mineral surface. This is consistent with higher Fe solubility of 1.2% as compared to that of the highly reactive Fe (0.63%) (Shi et al., 2011). Only 3.3% of Fe was dissolved at a dust/liquid ratio of 10 g L^{-1} and pH 2, and Fe dissolution stopped at 180 h. The calculated solubility of the second Fe pool is –3.55 (mol L^{-1}). The above experimental dataset is used to determine the model parameters to predict the influence of solution saturation state on the Fe dissolution rates (see Table 3 and discussion below).

Based on above laboratory results (Figs. 2 and 3), Fe dissolution from mineral dust aerosols is treated explicitly as a kinetic process that depends on the pH, ambient temperature, the degree of solution saturation, and competition for oxalate between surface Fe and dissolved Fe in our model (Table 3). The net Fe dissolution rates (ΣRFe_i in units of moles of dissolved Fe per Fe gram of Fe-containing mineral particle per second) for the proton-promoted (i = 1), oxalate-promoted (i = 2), and quasi-photo-reductive (i = 3) Fe dissolution schemes can be empirically described using the following equation, which is similar to the formulation applied for Fe-containing minerals (Zhang et al., 1985; Lasaga et al., 1994; Hamer et al., 2003; Meskhidze et al., 2005; Lanzl et al., 2012; Ito and Xu, 2014; Ito, 2015):

$$RFe_i = k_i(\mathrm{pH, T}) \times a(H^+)^{mi} \times f_i \times g_i \quad (1)$$

where k_i is the 'far-from-equilibrium' (i.e., $f_i = 1$ and $g_i = 1$) Fe release rate (moles Fe g^{-1} s^{-1}), $a(H^+)$ is the H^+ activity, m_i represents the empirical reaction order for protons, and f_i and g_i account for the suppression.

The Fe release rate, k_i, is estimated for the proton- and oxalate-promoted dissolution schemes by fitting the parameters to our measurements in sulfuric acid and ammonium sulfate (experiment (2) and (3)) with and without oxalate (Fig. 2). Fe release from mineral dust under acidic conditions is characterized by initial rapid Fe release and subsequent slow Fe release (Desboeufs et al., 1999; Mackie et al., 2005; Cwiertny et al., 2008; Shi et al. 2011). Since the typical lifetime of mineral dust is about a week, the initial rapid Fe release rates are important for the atmospheric processing of mineral dust. A three-stage kinetic model is used to describe the Fe release behavior of mineral dust: 1st stage is characterized by a rapid dissolution of hydrous ferric oxide (HFO) on the surface of minerals, 2nd stage is an intermediate stage of nano-sized Fe oxides dissolution from the surface of minerals, and 3rd stage is the Fe release from fine-grained materials, which are internally mixed with aluminosilicate particles, as the mineral surface is slowly dissolved. Here, we prescribe the content of HFO (0.65%) and nano-sized Fe oxides (1.3%) on the surface of minerals. The content of HFO is similar to that of the highly reactive Fe measured on the mineral surface and within the range of the first Fe pool from 0.5% to 2.9% (Shi et al., 2011). The content of nano-sized Fe oxides is also within the range of the second Fe pool from 1.0% to 3.5%. The proton-promoted dissolution rates for stage I and II are strongly dependent on pH. A comparable strong dependence on pH was also reported for nano-sized hematite (Lanzl et al., 2012). The similarity in our Fe release rates to those of illite suggests that Fe is mainly released from the reactive surface on Fe-containing minerals by similar mechanisms to alminosilicates (Fig. S2), which involve inward movement of dissolution from the grain edges (Brandt et al., 2003; Rozalén et al., 2008). Consequently, we can avoid the need to explicitly treat individual Fe-containing minerals to represent dissolution processes that occur on the timescale of aerosol lifetime by using equation (1), which is similar to the treatment applied for combustion aerosols (Ito, 2015).

The enhanced mineral dissolution in the presence of chelating ligands such as oxalate has been attributed to both the ligand adsorption at the surface of mineral and complex formation in solution (Drever and Stillings, 1997). The differences between with (i.e., measured overall rate) and with no oxalate (i.e., proton-promoted dissolution rate) can be attributed to the surface complexation (i.e., oxalate-promoted dissolution rate). We observed rates of oxalate-promoted dissolution to be almost independent of pH for stage I and III (Table 3), but could not calculate the empirical reaction order for stage II from the measurements. Lanzl et al. (2012) found that this value was nearly independent of pH (< 4.0) and particle size between 8 nm and 90 nm hematite (Zhang et al., 1985). Thus we apply the same value to stage II as in stage I. The calculations (red squares) reproduce the initial rapid Fe release and subsequent slow Fe release due to the proton- and oxalate-promoted Fe dissolution. The calculations also reproduce the enhancement in the Fe solubility due to the effects of oxalate under acidic conditions, compared with proton-promoted dissolution, as was observed for Arizona test dust in previous study (Chen and Grassian, 2013). The activation energy for k_i is described by a function of pH and temperature for soils (Bibi et al., 2014). The Fe release is suppressed by the degree of saturation, f_i, and competition for oxalate between surface Fe and dissolved Fe, g_i, (Ito, 2015). We apply the same equation for mineral dust, g_i, as in Ito (2015). Thus excess oxalate is needed to form mononuclear bidentate ligand with surface Fe and promote Fe dissolution significantly (Chen and Grassian, 2013). The function f_i ($0 \leq f_i \leq 1$) is given by

$$f_i = 1 - (a_{Fe} \times a_H^{-ni}) / Keq_i \qquad (2)$$

in which a_{Fe} is the concentration of Fe^{3+} in aerosol water (mol L^{-1}), n_i is the stoichiometric ratio, and Keq_i is the equilibrium constant measured.

Results of previous laboratory experiments in batch experiments showed that oxalate had negligible effect on the Fe dissolution of hematite at higher pH values (≥ pH = 5) under dark conditions (Zhang et al., 1985; Xu and Gao, 2008; Lanzl et al., 2012). The decrease in proton concentration (e.g., during activation into cloud droplets or neutralization by carbonate) could lead to formation of the amorphous $Fe(OH)_3(s)$ that coats on the mineral surfaces (Shi et al., 2009, 2015) and inhibits both the adsorption of oxalate and the detachment of surface Fe-oxalate (Zhang et al., 1985; Jang et al., 2007; Rozalén et al., 2014). This effect was not considered in previous modeling studies for mineral dust, which could calculate enhanced Fe solubility at higher pH (≥ 3) due to oxalate-promoted dissolution (Luo and Gao, 2010; Johnson and Meskhidze, 2013; Myriokefalitakis et al., 2015).

Paris et al. (2011) concluded that the light-induced reductive dissolution was not the principal process to explain the increase in Fe solubility under low dissolved Fe and low oxalate concentrations. However, the Fe release from the reactive surface on Fe-containing minerals was observed at higher pH values (≥ 5) under high dissolved Fe and high oxalate concentrations and irradiation conditions (Lanzl et al., 2012; Chen and Grassian, 2013). Two rate-limiting steps are possibly involved in apparent contradictions at higher pH: the adsorption of oxalate on the oxide surfaces at low dissolved Fe concentration (i.e., far from dissolution equilibrium) and the detachment of surface Fe-oxalate via photo-induced ligand-to-metal charge transfer as dissolution equilibrium is approached (Kraemer and Hering, 1997). To examine the uncertainty in Fe release at higher pH values, no pH effect on the suppression of quasi-photo-induced Fe dissolution for mineral aerosols was performed in the sensitivity simulation. In analogy to the combustion aerosols (Chen and Grassian, 2013; Ito, 2015), we apply the same rate constant to quasi-photo-induced dissolution as in oxalate-promoted dissolution and we set $f_3 = 1$ in equation (1). The quasi-photo-induced dissolution rate is calculated by scaling the photolysis rate of H_2O_2 estimated in the model, following Ito (2015). The photo-degradation of oxalate due to photolysis of Fe-oxalate complexes is simulated for Fe-containing aerosols in aqueous chemistry (Lin et al., 2014; Ito, 2015).

5. Modeling results and discussion

The model-calculated concentrations of total and soluble Fe in aerosols have been extensively compared with field observations (Ito and Feng, 2010; Ito, 2012, 2013, 2015; Ito and Xu, 2014). Here, model-calculated daily average surface concentrations of soluble Fe (red squares) were compared with the measurements (black circles) during the 2010 and 2011 U.S. GEOTRACES cruises over the North Atlantic (Fig. 4) (Wozniak et al., 2013, 2015). The model-calculated variability at each latitude and longitude represents the daily variability during the sampling dates. The modeled soluble Fe concentration exhibits a latitudinal variability, which is similar to that of the measurements, with low values over the remote ocean (<0.5 ng m^{-3}), intermediate values near European continents, and high values near North African continents (>5 ng m^{-3}) (Fig. 4a). The modeled soluble Fe concentration shows a longitudinal variability, which is also similar to that of the measurements, with low values over the remote ocean (<0.5 ng m^{-3}), intermediate values near North American continents, and high values near North African continents (>2 ng m^{-3}) (Fig. 4b).

Figure 5 displayed the daily averaged, model-calculated surface total aerosol Fe loading, Fe solubility, Fe/WSOC molar ratio, and dust/combustion ratio for soluble Fe (red squares) over the 2010 and 2011 US GEOTRACES cruise tracks in comparison with the measurements (black circles) by Wozniak et al. (2013, 2015). As previously reported in Ito (2013), the oil combustion from shipping mainly contributes to high Fe solubility at low Fe loading observed over the high latitude North Atlantic Ocean (Fig. 5a). In this study, low Fe solubility near North African continent was successfully simulated. The internal mixing of alkaline minerals with Fe-containing minerals in aqueous chemistry for mineral dust can lead to higher pH and thus suppress the Fe dissolution near the source regions, compared to the external mixing (Ito and Feng, 2010). The model predicts relatively higher pH values for dust aerosols except submicron particles near the source regions, because the dust alkalinity reservoir (i.e., calcite) is able to buffer the acidification (Fig. S3). While our model has incorporated the initial rapid Fe release rate in acid solutions with oxalate explicitly, the comparisons with observations support the suppression of Fe dissolution under low acidity and low oxalate concentration near the source region of dust aerosols.

The Fe/WSOC molar ratios in aerosols influenced by combustion aerosols are 2–3 orders of magnitude lower than those near North African continent, which are also consistent with the observations (Wozniak et al., 2013, 2015) (Fig. 5b). The averaged WSOC concentration in our model (330±470 ng m^{-3}) is consistent with the measurements (330±290 ng m^{-3}). The higher Fe solubility measured in water (pH = 5.5) for the excess WSOC with Fe-binding functionalities (e.g., –COOH, $–NH_2$) may suggest a potential role of the organic compounds in aerosols for the delivery of Fe to the ocean in soluble form (Wozniak et al., 2013, 2015). Here, similar plots can be obtained even with a constant WSOC concentration at 330 (ng m^{-3}) (Fig. S4). The results indicate that the variability in Fe solubility is nearly independent of the variability in WSOC concentration, possibly because of the excess ligands to stabilize Fe in solution at low Fe loading.

The use of our process-based model demonstrates that chemical reactions and mixing with combustion aerosols are the main mechanisms to cause the high Fe solubility at low Fe loading in the North Atlantic (Fig. 5c). As previously discussed in Ito (2013), this is consistent with the observations (e.g., Sedwick et al., 2007; Séguret et al., 2011).

The suppression of Fe dissolution under low proton and low oxalate concentrations leads to the lower Fe solubility of mineral dust deposited to the ocean (0.64%–0.71%) on a global mean in present days (Table 4), compared to those estimated for mineral dust by previous modeling studies (1.4%–15%, see Table 5 in Hajima et al., 2014). The Fe solubility for mineral dust varies spatially over the remote oceans, due to the proton-, oxalate-promoted, and quasi-photo-reductive Fe dissolution (Fig. 6). The Fe solubility ranges from 0.75 to 2% over the North Atlantic and Pacific in present days (Fig. 6a and 6c), which is relatively consistent with that (1%–2%) used in conventional ocean biogeochemical models (Jickells et al. 2005). The base simulations result in low Fe solubility (<1%) over the Southern Ocean in present days and significant portions of the ocean in preindustrial era, due to the suppression of Fe dissolution under low proton concentrations (Fig. 6a and 6b). In contrast, the sensitivity simulations for mineral aerosols (i.e., $f_3 = 1$) lead to higher Fe solubility (>1%) deposited to the remote oceans of high nitrate, low chlorophyll (HNLC) regions such as the subarctic north Pacific, the east equatorial Pacific, and the Southern Ocean, when quasi-photo-reductive dissolution was considered at higher pH values (Fig. 6c and 6d). This is reflected in higher contribution of oxalate-promoted (i = 2 and 3) dissolution to total soluble Fe deposition in the sensitivity simulations for mineral aerosols, compared to that (i = 2) in the base simulations (Fig. S5). We note that higher contribution of proton-promoted (i = 1) dissolution near the source regions may include the effect of oxalate on Fe dissolution via the suppression of mineral dissolution as well as the soluble Fe content at emission. As a result, the proton-promoted dissolution scheme contributed the majority of soluble Fe deposition to the ocean, 90% for the base case and 69% for the sensitivity case, respectively. Since this Fe dissolution is not only due to the proton-promoted dissolution by definition, we also examined the effect of different assumption on the initial period of enhanced Fe release in an additional sensitivity simulation, in which we use 0.1% for the initial Fe solubility of mineral dust (Hand et al., 2004; Ito and Xu, 2014). The model results show that the contribution of dissolution scheme to total soluble Fe deposition depends on the assumption on the initial Fe solubility at emission (Fig. S6). The model results suggest that the initial soluble Fe content from dust source regions such as South America (Patagonia), Australia, and southern Africa may be important for the supply of soluble Fe to the Southern Ocean. The proton-promoted dissolution scheme contributed 77% for the additional sensitivity case, which is between our base and sensitivity simulations.

The annually averaged rate of deposition of soluble Fe from dust and combustion sources to the oceans is presented in Fig. 7a and 7d for the base and sensitivity simulations, respectively. The total Fe solubility (Fig. 7b and 7e) is higher than that calculated from dust only over significant portions of the open ocean. However, our modeled Fe solubility (0.1%–0.5% and 0.2%–0.7% for the base and sensitivity simulations, respectively) is still low over the South Atlantic east downwind from the Patagonian dust source regions where previous modeled Fe solubility deposited to the ocean (1.4%–2.0% by Mahowald et al., 2009; 0.5%–0.6% by Johnson et al., 2010) was significantly lower than that deduced from observations (7.5%–20% by Baker et al., 2013). Our modeled Fe solubility for dry deposition over the Atlantic (1.1%±1.9% and 1.2%±2.0%) is in good agreement with the measurement (2.1%±2.2%), while that for wet deposition (3.4%±3.2% and 3.6%±3.3%) is significantly lower than the measurement

(10.4%±4.6%) (Baker et al., 2013). Moreover, our monthly averaged Fe solubility (1%–4%) in wet deposition is an order of magnitude lower than that observed on the Kerguelen Islands in South Indian Ocean (82%±18% by Heimburger et al., 2013). This enhanced solubility may be due to unidentified reactive organic species in cloud and rain water, which contain Fe-binding functionalities (e.g., –COOH, $-NH_2$) such as humic-like substances from biomass burning and biologically derived materials from the ocean (Parazols et al. 2006; Deguillaume et al., 2014; Ito et al., 2014, 2015). The role of humic-like substances in the complexation and dissolution of Fe oxides over a wide pH range has received considerable attention in recent literatures (Al-Abadleh, 2015). The multiple ligands with high affinity for Fe binding can wrest aqueous Fe from any Fe-oxalate complexes, allow the oxalate ligand to react with the surface Fe oxides, and assist the Fe-oxalate detachment from the surface Fe oxides at intermediate pH (e.g., pH = 5) (Cheah et al., 2003). Thus the consumption of oxalate due to photolysis of the Fe-oxalate complex may be limited due to complexation with stronger ligands in atmospheric water. On the other hand, functional groups on the humic molecule are less protonated at pH > 4, increase the probability of coating of organic matters on the reactive mineral surfaces, and thus inhibit the oxalate-promoted dissolution (Drever and Stillings, 1997). Clearly, more work is required to elucidate the underlying mechanisms that promote Fe dissolution in cloud and rain water over the Southern Ocean in future studies.

The contributions of anthropogenic soluble Fe deposition to the present-days are examined in Fig. 7c and 7f for the base and sensitivity simulations, respectively. The soluble Fe deposition from both mineral dust and fossil fuel combustion sources due to changes in atmospheric pollution contributes more than half of the total soluble Fe deposition over significant portions of the open ocean in the Northern Hemisphere for the base simulations. The sensitivity simulations for mineral aerosols (i.e., $f_3 = 1$) lead to higher soluble Fe deposition in both present days and preindustrial era (Table 4) and result in lower anthropogenic soluble Fe deposition to the HNLC regions, due to almost no pH dependency of the quasi-photo-reductive dissolution. Of the total soluble Fe deposition from anthropogenic sources (excluding biomass burning) to the ocean (0.05–0.06 Tg Fe yr^{-1}), 67%–72% is from dust sources, 28%–33% is from fossil fuel combustion (Table 4). In contrast, our model indicated higher contribution of biomass burning aerosols in preindustrial era (42%–55% in total soluble Fe deposition to the ocean). However, significant uncertainties remain on the magnitude of this source strength (Luo et al., 2008; Ito, 2011, 2012, 2015; Wang et al., 2015). It should be noted that anthropogenic soluble Fe input is also sensitive to the soluble Fe content at emission. The additional sensitivity simulation with the initial Fe solubility (0.1%) for dust aerosols indicates smaller contribution of anthropogenic component near the source regions (Fig. S7).

Our estimate of total Fe deposition to the ocean (10 Tg Fe yr^{-1}) is within the range of other models (Table 5). Our estimates of soluble Fe deposition to the oceans (0.05 and 0.07 Tg Fe yr^{-1} from the base and sensitivity simulations, respectively) in preindustrial era are in good agreement with that of Myriokefalitakis et al. (2015) (Table 5). The ratio of present-day soluble Fe deposition to the preindustrial era from the base simulation (47%) is in good agreement with that estimated by Luo et al. (2008) (46%), despite the use of various dissolution schemes, emission data sets, and atmospheric transport models. The sensitivity simulations, which include the quasi-photo-reductive dissolution for mineral aerosols (i.e., $f_3 = 1$), results in relatively small increases in the soluble Fe deposition in the global ocean (0.077 and 0.122 Tg Fe yr^{-1} on a global mean in preindustrial and present days, respectively). The global deposition is similar between our base and sensitivity simulations, mainly because of the suppression of proton-promoted (i.e.,

f_1) and oxalate-promoted (i.e., g_2) dissolution near the strong source regions of mineral dust. This is reflected in lower Fe solubility (1.1%–1.2% on a global mean), compared to those estimated by previous modeling studies (1.4%–15%, see Table 5 in Hajima et al., 2014).

6 Conclusions

We have developed a new scheme of Fe dissolution, which reproduced the proton- and oxalate-promoted dissolution behaviors of our experimental results for mineral dust. The batch dissolution experiments provided the Fe dissolution rates under far from equilibrium conditions and the parameters for degree of suppression as the saturation state approached equilibrium. Our model reproduced the slope of Fe solubility vs. total Fe loading measured over the North Atlantic Ocean. To investigate the uncertainty in the Fe dissolution associated with organic compounds, negligible pH effect on the quasi-photo-induced Fe dissolution for mineral aerosols was performed in the sensitivity simulations. The Fe release scheme allows us to reduce the number of mineral tracers for implementation in the Earth system models. At lower proton activity and lower oxalate concentration in aerosol water on dust particles near major dust sources, both proton and oxalate had no significant effect on the Fe dissolution in our model and thus resulted in the lower Fe solubility of mineral dust deposited to the ocean (0.64%–0.71%) on a global mean in present days. Fe release under more acidic condition in aerosol water due to air pollution resulted in significant increases in soluble Fe deposition over large portions of the open ocean in the Northern Hemisphere. In our model, low Fe solubility is estimated for mineral dust (< 1%) over the Southern Ocean downwind from the dust source regions. The differences between our base and sensitivity simulations for mineral aerosols are notable for low Fe loading over the remote HNLC regions such as the subarctic north Pacific, the east equatorial Pacific, and the Southern Ocean. However, the differences in Fe solubility between different simulations are generally smaller than the differences between different model estimates and measurements. A comprehensive comparison of model predicted Fe and its related species with observations is therefore needed to elucidate the high Fe solubility observed under pristine conditions.

Acknowledgments. Support for this research was provided to A. Ito by Program for Risk Information on Climate Change (MEXT). All of the numerical simulations were performed using the SGI ICE X at the JAMSTEC. Z. Shi is supported by UK Natural Environment Research Council (NE/I021616/1, NE/K000845/1) and the Royal Society. We would like to thank E. Journet and Y. Balkanski for making the mineralogical database available. We are grateful to R. Shelley, L. William, and their colleagues for kindly providing the observational data set during the 2010 U.S. GEOTRACES cruise, supported by NSF, USA, OCE-0752832, 0929919, and 1132766. The authors would like to thank the two anonymous reviewers for their constructive comments.

References

Al-Abadleh, H. A.: Review of the bulk and surface chemistry of iron in atmospherically relevant systems containing humic-like substances (HULIS), RSC Adv., 5, 45785–45811, doi:10.1039/c5ra03132j, 2015.

Amram, K. and Ganor, J.: The combined effect of pH and temperature on smectite dissolution rate under acidic conditions, Geochim. Cosmochim. Acta, 69, 2535–2546, doi:10.1016/j.gca.2004.10.001, 2005.

Baker, A. R., Adams, C., Bell, T. G, Jickells, T. D., and Ganzeveld, L.: Estimation of atmospheric nutrient inputs to the Atlantic Ocean from 50°N to 50°S based on large-scale field sampling: Iron and other dust-associated elements, Global Biogeochem. Cy., 27, 755–767, doi: 10.1002/gbc.20062, 2013.

Bibi, I., Singh, B., and Silvester, E.: Dissolution of illite in saline–acidic solutions at 25°C, Geochim. Cosmochim. Acta, 75, 3237–3249, doi:10.1016/j.gca.2011.03.022, 2011.

Bibi, I., Singh, B., and Silvester, E.: Dissolution kinetics of soil clays in sulfuric acid solutions: Ionic strength and temperature effects, Appl. Geochem., 51, 170–183, doi:10.1016/j.apgeochem.2014.10.004, 2014.

Bonneville, S., Van Cappellen, P., and Behrends, T.: Microbial reduction of iron(III) oxyhydroxides: effects of mineral solubility and availability, Chem. Geol., 212, 255–268, doi:10.1016/j.chemgeo.2004.08.015, 2004.

Brandt, F., Bosbach, D., Krawczyk-Bärsch, E., Arnold, T., and Bernhard, G.: Chlorite dissolution in the acid pH-range: A combined microscopic and macroscopic approach, Geochim. Cosmochim. Acta, 67, 1451–1461, doi:10.1016/S0016-7037(02)01293-0, 2003.

Cama, J. and Ganor, J.: The effects of organic acids on the dissolution of silicate minerals: A case study of oxalate catalysis of kaolinite dissolution, Geochim. Cosmochim. Acta, 70(9), 2191–2209, doi:10.1016/j.gca.2006.01.028, 2006.

Ciais, P., Sabine, C., Govindasamy, B., Bopp, L., Brovkin, V., Canadell, J., Chhabra, A., DeFries, R., Galloway, J., Heimann, M., Jones, C., Le Quéré, C., Myneni, R., Piao, S., and Thornton, P.: Chapter 6: Carbon and Other Biogeochemical Cycles, in: Climate Change 2013 The Physical Science Basis, edited by: Stocker, T., Qin, D., and Platner, G.-K., Cambridge University Press, Cambridge, 2013.

Cheah, S. F., Kraemer, S. M., Cervini-Silva, J., & Sposito, G.: Steady-state dissolution kinetics of goethite in the presence of desferrioxamine B and oxalate ligands: implications for the microbial acquisition of iron. Chem. Geol., 198(1), 63-75 doi:10.1016/S0009-2541(02)00421-7, 2003.

Chen, H. and Grassian, V. H.: Iron dissolution of dust source materials during simulated acidic processing: The effect of sulfuric, acetic, and oxalic acids, Environ. Sci. Technol., 47, 10312−10321, doi:10.1021/es401285s, 2013.

Cornell, R. M. and Schwertmann, U.: The iron oxides: Structure, properties, reactions, occurrence and uses, Wiley-VCH publishers, New York, 2003.

Cwiertny, D. M., Baltrusaitis, J., Hunter, G. J., Laskin, A., Scherer, M. M., and Grassian, V. H.: Characterization and acid-mobilization study of iron-containing mineral dust source materials, J. Geophys. Res., 113, D05202, doi:10.1029/2007jd009332, 2008.

Deguillaume, L., Desboeufs, K. V., Leriche, M., Long, Y., and Chaumerliac, N.: Effect of iron dissolution on cloud chemistry: from laboratory measurements to model results, Atmos. Pollut. Res, 1(4), 220–228, doi:10.5094/APR.2010.029, 2010.

Deguillaume, L., Charbouillot, T., Joly, M., Vaïtilingom, M., Parazols, M., Marinoni, A., Amato, P., Delort, A.-M., Vinatier, V., Flossmann, A., Chaumerliac, N., Pichon, J. M., Houdier, S., Laj, P., Sellegri, K., Colomb, A., Brigante, M. , and Mailhot, G.: Classification of clouds sampled at the puy de Dôme (France) based on 10 yr of monitoring of their physicochemical properties, Atmos. Chem. Phys., 14, 1485–1506, doi:10.5194/acp-14-1485-2014, 2014.

Desboeufs, K., Losno, R., Vimeux, F., and Cholbi, S.: pH dependent dissolution of wind transported Saharan dust, J. Geophys. Res., 104, 21287–21299, 1999.

Drever, J. I. and Stillings, L. L.: The role of organic acids in mineral weathering, Colloids Surfaces A, 120, 167–181, 1997.

Feng, Y. and Penner, J. E.: Global modeling of nitrate and ammonium: Interaction of aerosols and tropospheric chemistry, J. Geophys. Res., 112, D01304, doi:10.1029/2005JD006404, 2007.

Golubev, S. V., Bauer, A., and Pokrovsky, O. S.: Effect of pH and organic ligands on the kinetics of smectite dissolution at 25°C, Geochim. Cosmochim. Acta, 70(17), 4436–4451, doi:10.1016/j.gca.2006.06.1557, 2006.

Hajima, T., Kawamiya, M., Watanabe, M., Kato, E., Tachiiri, K., Sugiyama, M., Watanabe, S., Okajima, H., and Ito, A.: Modeling in Earth system science up to and beyond IPCC AR5, Progress in Earth and Planetary Science, 1, 1–25, doi:10.1186/s40645-014-0029-y, 2014.

Hamer, M., Graham, R., Amrhein, C., and Bozhilov, K.: Dissolution of ripidolite (Mg, Fe-chlorite) in organic and inorganic acid solutions, Soil Sci. Soc. Am. J., 67 (2), 654−661, 2003.

Hand, J. L., Mahowald, N. M., Chen, Y., Siefert, R. L., Luo, C., Subramaniam, A., and Fung, I.: Estimates of atmosphericprocessed soluble iron from observations and a global mineral aerosol model: Biogeochemical implications, J. Geophys. Res., 109, D17205, doi:10.1029/2004JD004574, 2004.

Heimburger, A., Losno, R., and Triquet, S.: Solubility of iron and other trace elements in rainwater collected on the Kerguelen Islands (South Indian Ocean), Biogeosciences, 10, 6617-6628, doi:10.5194/bg-10-6617-2013, 2013.

Ito, A.: Mega fire emissions in Siberia: potential supply of bioavailable iron from forests to the ocean, Biogeosciences, 8, 1679–1697, doi:10.5194/bg-8-1679-2011, 2011.

Ito, A.: Contrasting the effect of iron mobilization on soluble iron deposition to the ocean in the Northern and Southern Hemispheres, J. Meteorol. Soc. Japan, 90A, 167–188, DOI:10.2151/jmsj.2012-A09, 2012.

Ito, A.; Global modeling study of potentially bioavailable iron input from shipboard aerosol sources to the ocean, Global Biogeochem. Cy., 27, 1–10, doi: 10.1029/2012GB004378, 2013.

Ito, A.: Atmospheric processing of combustion aerosols as a source of bioavailable iron, Environ. Sci. Technol. Lett., 2 (3), 70–75, doi: 10.1021/acs.estlett.5b00007, 2015.

Ito, A. and Feng, Y.: Role of dust alkalinity in acid mobilization of iron, Atmos. Chem. Phys., 10, 9237–9250, doi:10.5194/acp-10-9237-2010, 2010.

Ito, A., Kok, J., Feng, Y., and Penner, J.: Does a theoretical estimation of the dust size distribution at emission suggest more bioavailable iron deposition?, Geophys. Res. Lett., 39, L05807, doi:10.1029/2011GL050455, 2012.

Ito, A., Lin, G., Penner, J. E.: Reconciling modeled and observed atmospheric deposition of soluble organic nitrogen at coastal locations, Global Biogeochem. Cy., 28, 617–630, doi:10.1002/2013GB004721, 2014.

Ito, A., Lin, G., and Penner, J. E.: Global modeling study of soluble organic nitrogen from open biomass burning, Atmos. Environ., 121, 103–112, 10.1016/j.atmosenv.2015.01.031, 2015.

Ito, A. and Xu, L.: Response of acid mobilization of iron-containing mineral dust to improvement of air quality projected in the future, Atmos. Chem. Phys., 14, 3441–3459, doi:10.5194/acp-14-3441-2014, 2014.

Jang, J. H., Dempsey, B. A., and Burgos, W. D.: Solubility of hematite revisited: Effects of hydration, Environ. Sci. Technol., 41(21), 7303–7308, doi:10.1021/es8010139, 2007.

Jickells, T. D., An, Z. S., Andersen, K. K., Baker, A. R., Bergametti, G., Brooks, N., Cao, J. J., Boyd, P. W., Duce, R. A., Hunter, K. A., Kawahata, H., Kubilay, N., LaRoche, J., Liss, P. S., Mahowald, N., Prospero, J. M., Ridgwell, A. J., Tegen, I., and Torres, R.: Global iron connections between desert dust, ocean biogeochemistry, and climate, Science, 308, 67–71, doi:10.1126/science.1105959, 2005.

Johnson, M. S., Meskhidze, N., Solmon, F., Gassó, S., Chuang, P. Y., Gaiero, D. M., Yantosca, R. M., Wu, S., Wang, Y., and Carouge, C.: Modeling dust and soluble iron deposition to the South Atlantic Ocean, J. Geophys. Res., 115, D15202, doi:10.1029/2009JD013311, 2010.

Johnson, M. S., and Meskhidze, N.: Atmospheric dissolved iron deposition to the global oceans: effects of oxalate-promoted Fe dissolution, photochemical redox cycling, and dust mineralogy, Geosci. Model Dev., 6, 1137–1155, doi:10.5194/gmd-6-1137-2013, 2013.

Journet, E., Desboeufs, K. V., Caquineau, S., and Colin, J.-L.: Mineralogy as a critical factor of dust iron solubility, Geophys. Res. Lett., 35, L07805, doi:10.1029/2007GL031589, 2008.

Journet, E., Balkanski, Y., and Harrison, S. P.: A new data set of soil mineralogy for dust-cycle modeling, Atmos. Chem. Phys., 14(8), 3801–3816, doi:10.5194/acp-14-3801-2014, 2014.

Kieber, R. J., Skrabal, S.A., Smith, B., and Willey, J. D.: Organic complexation of Fe(II) and its impact on the redox cycling of iron in rain, Environ. Sci. Technol., 39, 1576−1583, 2005.

Kok, J. F.: A scaling theory for the size distribution of emitted dust aerosols suggests climate models underestimate the size of the global dust cycle, P. Natl. Acad. Sci. USA, 108, 1016–1021, doi:10.1073/pnas.1014798108, 2011.

Kraemer, S. M. and Hering, J. G.: Influence of solution saturation state on the kinetics of ligand-controlled dissolution of oxide phases, Geochim. Cosmochim. Acta, 61(14), 2855–2866, 1997.

Lamarque, J.-F., Bond, T. C., Eyring, V., Granier, C., Heil, A., Klimont, Z., Lee, D., Liousse, C., Mieville, A., Owen, B., Schultz, M. G., Shindell, D., Smith, S. J., Stehfest, E., Van Aardenne, J., Cooper, O. R., Kainuma, M., Mahowald, N., McConnell, J. R., Naik, V., Riahi, K., and van Vuuren, D. P.: Historical (1850–2000) gridded anthropogenic and biomass burning emissions of reactive gases and aerosols: methodology and application, Atmos. Chem. Phys., 10, 7017–7039, doi:10.5194/acp-10-7017-2010, 2010.

Lanzl, C. A., Baltrusaitis, J., and Cwienty, D. M.: Dissolution of hematite nanoparticle aggregates: Influence of primary particle size, dissolution mechamism, and solution pH, Langmuir, 28, 15797–15808, doi:10.1021/la3022497, 2012.

Lasaga, A. C., Soler, J. M., Ganor, J., Burch, T. E., and Nagy, K. L.: Chemical-weathering rate laws and global geochemical cycles, Geochim. Cosmochim. Acta, 58(10), 2361–2386, 1994.

Lin, G., Sillman, S., Penner, J. E., and Ito, A.: Global modeling of SOA: the use of different mechanisms for aqueous-phase formation, Atmos. Chem. Phys., 14, 5451–5475, doi:10.5194/acp-14-5451-2014, 2014.

Lowson, R. T., Comarmond, M. C. J., Rajaratnam, G., and Brown, P. L.: The kinetics of the dissolution of chlorite as a function of pH and at 25°C, Geochim. Cosmochim. Acta, 69(7), 1687–1699, doi:10.1016/j.gca.2004.09.028, 2005.

Liu, X., Penner, J. E., and Herzog, M.: Global modeling of aerosol dynamics: Model description, evaluation and interactions between sulfate and non-sulfate aerosols, J. Geophys. Res., 110, D18206, doi:10.1029/2004JD005674, 2005.

Luo, C. and Gao, Y.: Aeolian iron mobilisation by dust-acid interactions and their implications for soluble iron deposition to the ocean: a test involving potential anthropogenic organic acidic species, Environ. Chem., 7, 153–161, doi:10.1071/EN09116, 2010.

Luo, C., Mahowald, N., Bond, T., Chuang, P. Y., Artaxo, P., Siefert, R., Chen, Y., and Schauer, J.: Combustion iron distribution and deposition, Global Biogeochem. Cy., 22, GB1012, doi:10.1029/2007GB002964, 2008.

Mackie, D. S., Boyd, P. W., Hunter, K. A., and McTainsh, G. H.: Simulating the cloud processing of iron in Australian dust: pH and dust concentration, Geophys. Res. Lett., 32, L06809, doi:10.1029/2004GL022122, 2005.

Mahowald, N. M., Engelstaedter, S., Luo, C., Sealy, A., Artaxo, P., Benitez-Nelson, C., Bonnet, S., Chen, Y., Chuang, P. Y., Cohen, D. D., Dulac, F., Herut, B., Johansen, A. M., Kubilay, N., Losno, R., Maenhaut, W., Paytan, A., Prospero, J. A., Shank, L. M., and Siefert, R. L.: Atmospheric iron deposition: Global distribution, variability, and human perturbations, Annu. Rev. Mar. Sci., 1, 245–278, doi:10.1146/annurev.marine.010908.163727, 2009.

Malmström, M., and Banwart, S.: Biotite dissolution at 25°C: The pH dependence of dissolution rate and stoichiometry, Geochim. Cosmochim. Acta, 61(14), 2779–2799, 1997.

Meskhidze, N., Chameides, W. L., Nenes, A., and Chen, G.: Iron mobilization in mineral dust: Can anthropogenic SO2 emissions affect ocean productivity?, Geophys. Res. Lett., 30, 2085, doi:10.1029/2003GL018035, 2003.

Meskhidze, N., Chameides, W. L., and Nenes, A.: Dust and pollution: A recipe for enhanced ocean fertilization?, J. Geophys. Res., 110, D03301, doi:10.1029/2004JD005082, 2005.

Myriokefalitakis, S., Daskalakis, N., Mihalopoulos, N., Baker, A. R., Nenes, A., and Kanakidou, M.: Changes in dissolved iron deposition to the oceans driven by human activity: a 3-D global modelling study, Biogeosciences, 12, 3973–3992, doi:10.5194/bg-12-3973-2015, 2015.

Nickovic, S., Vukovic, A., Vujadinovic, M., Djurdjevic, V., and Pejanovic, G.: Technical Note: High-resolution mineralogical database of dust-productive soils for atmospheric dust modeling, Atmos. Chem. Phys., 12, 845–855, doi:10.5194/acp-12-845-2012, 2012.

Paris, R., Desboeufs, K. V., and Journet, E.: Variability of dust iron solubility in atmospheric waters: Investigation of the role of oxalate organic complexation, Atmos. Environ., 45, 6510–6517, doi:10.1016/j.atmosenv.2011.08.068, 2011.

Parazols, M., Marinoni, A., Amato, P., Abida, O., Laj, P., and Mailhot, G.: Speciation and role of iron in cloud droplets at the puy de Dôme station, J. Atmos. Chem., 54(3), 267–281, doi:10.1007/s10874-006-9026-x, 2006.

Ramos, M. E., García-Palma, S., Rozalén, M., Johnston, C. T., and Huertas, F. J.: Kinetics of montmorillonite dissolution: An experimental study of the effect of oxalate, Chem. Geol., 363, 283–292, doi:10.1016/j.chemgeo.2013.11.014, 2014.

Rotman, D. A., Atherton, C. S., Bergmann, D. J., Cameron-Smith, P. J., Chuang, C. C., Connell, P. S., Dignon, J. E., Franz, A., Grant, K. E., Kinnison, D. E., Molenkamp, C. R., Proctor, D. D., and Tannahill, J. R.: IMPACT, the LLNL 3-D global atmospheric chemical transport model for the combined troposphere and stratosphere: Model description and analysis of ozone and other trace gases, J. Geophys. Res., 109, D04303, doi:10.1029/2002JD003155, 2004.

Rozalén, M. L., Huertas, F. J., Brady, P. V., Cama, J., García-Palma, S., and Linares, J.: Experimental study of the effect of pH on the kinetics of montmorillonite dissolution at 25°C, Geochim. Cosmochim. Acta, 72(17), 4224–4253, doi:10.1016/j.gca.2008.05.065, 2008.

Rozalén, M., Ramos, M. E., Fiore, S., Gervilla, F., and Huertas, F. J.: Effect of oxalate and pH on chrysotile dissolution at 25°C: An experimental study, Am. Mineral., 99(4), 589–600, doi:10.2138/am.2014.4636, 2014.

Rubasinghege, G., Lentz, R. W., Scherer, M. M., and Grassian, V. H.: Simulated atmospheric processing of iron oxyhydroxide minerals at low pH: roles of particle size and acid anion in iron dissolution, Proc. Natl. Acad. Sci. U. S. A., 107, 6628–6633, doi:10.1073/pnas.0910809107, 2010.

Scanza, R. A., Mahowald, N., Ghan, S., Zender, C. S., Kok, J. F., Liu, X., Zhang, Y., and Albani, S.: Modeling dust as component minerals in the Community Atmosphere Model: development of framework and impact on radiative forcing, Atmos. Chem. Phys., 15, 537–561, doi:10.5194/acp-15-537-2015, 2015.

Sedwick, P. N., Sholkovitz, E. R., and Church, T. M.: Impact of anthropogenic combustion emissions on the fractional solubility of aerosol iron: Evidence from the Sargasso Sea, Geochem. Geophys. Geosyst., 8, Q10Q06 doi:10.1029/2007GC001586, 2007.

Séguret, M. J. M., Koçak, M., Theodosi, C., Ussher, S. J., Worsfold, P. J., Herut, B., .Mihalopoulos, N., Kubilay, N., and Nimmo, M.: Iron solubility in crustal and anthropogenic aerosols: The Eastern Mediterranean as a case study. Mar. Chem., 126, 229–238, doi:10.1016/j.marchem.2011.05.007, 2011.

Shi, Z., Krom, M. D., Bonneville. S., Baker, A. R., Jickells, T. D., and Benning, L. G.: Formation of iron nanoparticles and increase in iron reactivity in the mineral dust during simulated cloud processing, Environ. Sci. Technol., 43, 6592–6596, doi:10.1021/es901294g, 2009.

Shi, Z., Bonneville, S., Krom, M., Carslaw K., Jickells, T., Baker, A., and Benning, L.: Iron dissolution kinetics of mineral dust at low pH during simulated atmospheric processing, Atmos. Chem. Phys., 11, 995–1007, doi:10.5194/acp-11-995-2011, 2011.

Shi, Z., Krom, M. D., Jickells, T. D., Bonneville, S., Carslaw, K. S., Mihalopoulos, N., Baker, A. R., and Benning, L. G.: Impacts on iron solubility in the mineral dust by processes in the source region and the atmosphere: A review, Aeolian Res., 5, 21–42, doi:10.1016/j.aeolia.2012.03.001, 2012.

Shi, Z., Krom, M. D., Bonneville, S., and Benning, L. G.: Atmospheric processing outside clouds increases soluble iron in mineral dust, Environ. Sci. Technol., 49, 1472−1477, doi:10/1021/es504623, 2015.

Solmon, F., Chuang, P. Y., Meskhidze, N., and Chen, Y.: Acidic processing of mineral dust iron by anthropogenic compounds over the north Pacific Ocean, J. Geophys. Res., 114, D02305, doi:10.1029/2008JD010417, 2009.

Sorooshian, A., Wang, Z., Coggon, M. M., Jonsson, H. H., and Ervens, B.: Observations of sharp oxalate reductions in stratocumulus clouds at variable altitudes: organic acid and metal measurements during the 2011 E-PEACE campaign, Environ. Sci. Technol., 47, 7747−7756, doi:10.1021/es4012383, 2013.

Spokes, J. L. and Jickells, T. D: Factors controlling the solubility of aerosol trace metals in the atmosphere and on mixing into seawater, Aqua. Geochem., 1, 355−374, 1996.

Wang, R., Balkanski, Y., Boucher, O., Bopp, L., Chappell, A., Ciais, P., Hauglustaine, D., Peñuelas, J., and Tao, S.: Sources, transport and deposition of iron in the global atmosphere, Atmos. Chem. Phys., 15, 6247–6270, doi:10.5194/acp-15-6247-2015, 2015.

Wang, Z., Sorooshian, A., Prabhakar, G., Coggon, M. M., and Jonsson, H. H.: Impact of emissions from shipping, land, and the ocean on stratocumulus cloud water elemental composition during the 2011 E-PEACE field campaign, Atmos. Environ., 89, 570–580, doi:10.1016/j.atmosenv.2014.01.020, 2014.

Wexler, A. S. and Clegg, S. L.: Atmospheric aerosol models for systems including the ions H^+, NH_4^+, Na^+, SO_4^{2-}, NO_3^-, Cl^-, Br^-, and H_2O, J. Geophys. Res. 107, 4207, doi:10.1029/2001jd000451, 2002.

Willey, J. D., Kieber, R. J., Humphreys, J. J., Rice, B. C., Hopwood, M. J., Avery, G. B. and Mead R. N.: The role of fossil fuel combustion on the stability of dissolved iron in rainwater, Atmos. Environ. 107, 187−193, 2015.

Wozniak, A. S., Shelley, R. U., Sleighter, R. L., Abdulla, H. A. N., Morton, P. L., Landing, W. M., and Hatcher, P. G.: Relationships among aerosol water soluble organic matter, iron and aluminum in European, North African, and Marine air masses from the 2010 US GEOTRACES cruise, Mar. Chem., 153, 24–33, doi:10.1016/j.marchem.2013.04.011, 2013.

Wozniak, A. S., Shelley, R. U., McElhenie, S. D., Landing, W. M., and Hatcher, P. G.: Aerosol water soluble organic matter characteristics over the North Atlantic Ocean: Implications for iron-binding ligands and iron solubility, Mar. Chem., 173, 162–172, doi:10.1016/j.marchem.2014.11.002, 2015.

Xu, N. and Gao, Y.: Characterization of hematite dissolution affected by oxalate coating, kinetics and pH, Appl. Geochem., 23, 783–793, doi:10.1016/j.apgeochem.2007.12.026, 2008.

Xu, L. and Penner, J. E.: Global simulations of nitrate and ammonium aerosols and their radiative effects, Atmos. Chem. Phys., 12, 9479–9504, doi:10.5194/acp-12-9479-2012, 2012.

Yoon, T. H., Johnson, S. B., Musgrave, C. B., and Brown, G. E.: Adsorption of organic matter at mineral/water interfaces: I. ATR-FTIR spectroscopic and quantum chemical study of oxalate adsorbed at boehmite/water and corundum/water interfaces, Geochim. Cosmochim. Acta, 68(22), 4505–4518, doi:10.1016/j.gca.2004.04.025, 2004.

Yu, J. Z., Huang, X.-F., Xu, J., and Hu, M.: When aerosol sulfate goes up, so does oxalate: Implication for the formation mechanisms of oxalate, Environ. Sci. Technol., 39, 128–133, doi:10.1021/es049559f, 2005.

Zhang, Y., Kallay, N., and Matijević, E.: Interactions of metal hydrous oxides with chelating agents. 7. Hematite-oxalic acid and -citric acid systems, Langmuir, 1, 201–206, 1985.

Zhuang, G., Yi, Z., Duce, R. A., and Brown, P. R.: Link between iron and sulphur cycles suggested by detection of Fe(II) in remote marine aerosols, Nature, 355, 537–539, 1992.

Figures Captions

Fig. 1 Comparison of Fe solubility in solution (%) measured at two different dust/liquid ratios of 1 g L^{-1} (red triangles) and 10 g L^{-1} (blue squares) in 0.05 mol L^{-1} sulfuric acid solution with 1 mol L^{-1} $(NH_4)_2SO_4$ (I = 3.15 mol kg^{-1}), and dust/liquid ratios of 60 mg L^{-1} (black circles) and 1 g L^{-1} (green diamonds) in 0.005 mol L^{-1} sulfuric acid solution without $(NH_4)_2SO_4$ (pH = 2.0).

Fig. 2 Comparison of Fe solubility in solution (%) predicted using equation (1) with our measured Fe dissolution rates **(a)** with no oxalate at pH = 2, 0.05M H_2SO_4, 1M $(NH_4)_2SO_4$, **(b)** with no oxalate at pH = 3, 0.005M H_2SO_4, 1M $(NH_4)_2SO_4$, **(c)** with oxalate at pH = 2.1, 0.05M H_2SO_4, 1M $(NH_4)_2SO_4$, and 0.03 M $Na_2C_2O_4$, **(d)** with oxalate at pH = 3, 0.005M H_2SO_4, 1M $(NH_4)_2SO_4$, and 0.03 M $Na_2C_2O_4$. The red squares are calculated using equation (1) from the rate constants used in this study at each hour. The black circles are our measured data. The values of pH in solution are calculated using E-AIM (Wexler and Clegg, 2002, http://www.aim.env.uea.ac.uk/aim/aim.php).

Fig. 3 Comparison of Fe solubility in solution (%) predicted using equation (1) with the measured Fe dissolution rates at pH = 2, 0.005M H_2SO_4, and dust/solution of **(a)** 60 mg L^{-1}, **(b)** 1 g L^{-1}, **(c)** 10 g L^{-1}, and **(d)** 50 g L^{-1}. The red squares are calculated using equation (1) from the equilibrium constant (mol^{2} kg^{-2}) used in this study at each hour. The black circles are our measured data. The fraction of total dissolved Fe present as Fe(III) is prescribed at pH = 2 (0.2) in this calculation to emulate the experimental conditions, while the photochemical redox cycling between Fe(III) and

Fe(II) in solution is explicitly simulated in our global model (Lin et al., 2014). The large fraction of Fe(II) in solution under the dark conditions is likely associated with the Fe dissolution of Fe(II)-containing solids (Cwienty et al., 2008). The initial fraction of Fe speciation is not critical in estimating the Fe redox speciation in aerosol water, because Fe(II) is quickly oxidized to Fe(III) in oxygenated water (Deguillaume et al., 2010).

Fig. 4 Comparison of simulated (red squares) and observed (black circles) soluble Fe concentration (ng m^{-3}) during **(a)** 2010 and **(b)** 2011 U.S. GEOTRACES cruise over the North Atlantic (Wozniak et al., 2013, 2015). The number of modeled data points (84) is larger than the measurements (37), because each daily average is calculated for each sampling date at each center of cruise location.

Fig. 5 **(a)** Atmospheric loading of total aerosol Fe (ng m^{-3}) versus Fe solubility for model estimates (red squares) and measurements (black circles) over the cruise tracks. **(b)** The Fe/WSOC molar ratio versus percent of soluble Fe in total Fe for model estimates (red squares) and measurements (black circles) over the cruise tracks. **(c)** The dust/combustion ratio for soluble Fe versus Fe solubility for model results over the cruise tracks. The measurements are obtained from Wozniak et al., (2013, 2015). The number of modeled data points (84) is larger than the measurements (37), because each daily average is calculated for each sampling date at each center of cruise location.

Fig. 6 Ratio (%) of the soluble to total Fe deposition for mineral dust in **(a)** present days from base simulations, **(b)** preindustrial era from base simulations, **(c)** present days from sensitivity simulations, and **(d)** preindustrial era from sensitivity simulations. The formation of the amorphous $Fe(OH)_3(s)$ suppresses the oxalate-promoted dissolution from mineral aerosols in the base simulations, while no such effect was considered for quasi-light-induced reductive dissolution in the sensitivity simulation (i.e., $f_3 = 1$).

Fig. 7 Deposition of soluble Fe (ng Fe m^{-2} s^{-1}) from dust and combustion sources to the oceans in present days, Fe solubility in present days, and ratio of increase from preindustrial to present to soluble Fe deposition in present days. The formation of the amorphous $Fe(OH)_3(s)$ suppresses the oxalate-promoted dissolution from mineral aerosols in the base simulations, while no such effect was considered for quasi-light-induced reductive dissolution in the sensitivity simulation (i.e., $f_3 = 1$).

Table 1. Summary of Fe dissolution experiments performed in this study.

Experiment	pH	Dust/liquid ratio (g L^{-1})	Ammonium salt	Oxalate
Experiment 1	1.3	1	0	0
Experiment 1	2.1	1	0	0
Experiment 2	2	1	1 mol L^{-1} $(NH_4)_2SO_4$	0
Experiment 2	3.1	1	1 mol L^{-1} $(NH_4)_2SO_4$	0
Experiment 2	0.9	1	3 mol L^{-1} NH_4Cl	0
Experiment 2	2	10	1 mol L^{-1} $(NH_4)_2SO_4$	0
Experiment 3	2	1	1 mol L^{-1} $(NH_4)_2SO_4$	0.03 mol L^{-1}
Experiment 3	2	1	1 mol L^{-1} $(NH_4)_2SO_4$	0.03 mol L^{-1}
Experiment 4	2	0.06	0	0
Experiment 4	2	10	0	0
Experiment 4	2	50	0	0

Table 2. Global Fe emission (Tg Fe yr^{-1}) estimated for different types of Fe-containing aerosols.

Species	Preindustrial era	Present day
Dust	69 (98%)	69 (98%)
Oil combustion	0 (0%)	0.022 (0.03%)
Coal combustion	0.28 (1.0%)	0.69 (1.0%)
Biomass burning	0.66 (0.9%)	0.66 (0.9%)
Total Fe	70	71

Note: the parentheses represent the percentage of each source of Fe to total Fe. The initial Fe solubility (58 ± 22%) is used to estimate primary soluble Fe emission for the oil combustion aerosols only (Ito, 2015). We also examined the initial Fe solubility of mineral dust (0.1%) in an additional sensitivity simulation (Hand et al., 2004; Ito and Xu, 2014). Insoluble Fe can be transformed to secondary soluble Fe via atmospheric processing of Fe-containing mineral dust (see the text) and combustion aerosols (Ito, 2015).

Table 3. Constants used to calculate Fe dissolution rates for mineral dust, based on laboratory experiments.

Stage	Species	Scheme	Rate Constant k_i(pH, T)[1]	m_i[3]	K_{eq}[4]	n_i[5]
I	Ferrihydrite	Proton	$7.13 \times 10^{-5}\exp[E(\mathrm{pH})^2 \times (1/298-1/T)]$	1.1	1550	3
II	Nano-Fe oxides	Proton	$1.43 \times 10^{-4}\exp[E(\mathrm{pH})^2 \times (1/298-1/T)]$	1.6	42	2.75
III	Aluminosilicates	Proton	$5.85 \times 10^{-8}\exp[E(\mathrm{pH})^2 \times (1/298-1/T)]$	0.76	3.3	2.85
I	Ferrihydrite	Oxalate	$4.61 \times 10^{-8}\exp[E(\mathrm{pH})^2 \times (1/298-1/T)]$	0.069	1550[6]	3[6]
II	Nano-Fe oxides	Oxalate	$1.28 \times 10^{-8}\exp[E(\mathrm{pH})^2 \times (1/298-1/T)]$	0.069	1550[6]	3[6]
III	Aluminosilicates	Oxalate	$1.68 \times 10^{-9}\exp[E(\mathrm{pH})^2 \times (1/298-1/T)]$	0.056	1550[6]	3[6]
I	Ferrihydrite	Phot	$4.61 \times 10^{-8}\exp[E(\mathrm{pH})^2 \times (1/298-1/T)]$	0.069		
II	Nano-Fe oxides	Phot	$1.28 \times 10^{-8}\exp[E(\mathrm{pH})^2 \times (1/298-1/T)]$	0.069		
III	Aluminosilicates	Phot	$1.68 \times 10^{-9}\exp[E(\mathrm{pH})^2 \times (1/298-1/T)]$	0.056		

[1] k_i(pH, T) is the pH- and temperature-dependent ‘far-from-equilibrium’ Fe dissolution rate of Fe-containing mineral dust (moles Fe g^{-1} s^{-1}) for each Fe dissolution scheme *i*. The parameters are fit to our measurements for African dust. The photo-induced dissolution rate of Fe compounds is scaled to the photolysis rate of H_2O_2 calculated in the model, following Ito (2015).

[2] $E(pH) = -1.56 \times 10^3 \times pH + 1.08 \times 10^4$. The parameters are fit to the measurements for soils (Bibi et al., 2014).

[3] m_i is the reaction order with respect to aqueous phase protons, which was determined by linear regression from our experimental data in the pH range between 2 and 3 for proton- and oxalate-promoted dissolution schemes.

[4] *Keq* is the equilibrium constant (mol^2 kg^{-2}) (Bonneville et al., 2004; Jang et al., 2007).

[5] n_i is the stoichiometric ratio (Bonneville et al., 2004; Jang et al., 2007). The stoichiometric number of moles of Fe per mole of mineral is empirically determined for Fe dissolution rate as in the equation (1).

[6] The formation of the amorphous $Fe(OH)_3(s)$ suppresses the oxalate-promoted dissolution from mineral aerosols in the base simulations, while no such effect was considered for quasi-light-induced reductive dissolution in the sensitivity simulation (i.e., $f_3 = 1$).

Table 4. Annual deposition rates of total and soluble Fe (Tg Fe yr^{-1}) from different sources to the ocean in the base and sensitivity simulations.

Source	Fe deposition		Soluble Fe deposition	
	Preindustrial era	Present day	Preindustrial era	Present day
Dust in base case	9.9	9.9	0.018	0.063
Dust in sensitivity case	9.9	9.9	0.034	0.070
Dust in an additional sensitivity case*	9.9	9.9	0.027	0.069
Biomass burning	0.12	0.12	0.028	0.026
Coal combustion	0.051	0.14	0.0046	0.011
Oil Combustion	0	0.017	0	0.011

* Assuming an initial Fe solubility of 0.1%.

Table 5. Comparison of total and soluble Fe deposition to the oceans (Tg Fe yr^{-1}) from different studies for the preindustrial era and the present day.

Study	Total Fe	Soluble Fe (preindustrial)	Soluble Fe (current)
Base simulation	10	0.051	0.11
Sensitivity simulation	10	0.067	0.12
Luo et al. (2008)	11	0.10	0.21
Myriokefalitakis et al. (2015)	7.0	0.063	0.19
Jickells et al. (2005)	16		0.16–0.32
Ito (2015)	13		0.34
Wang et al. (2015)	8.4		0.17
Other models[1]	11–21		0.26–2.3

[1] The values are taken from a compilation of literatures (Hajima et al., 2014).

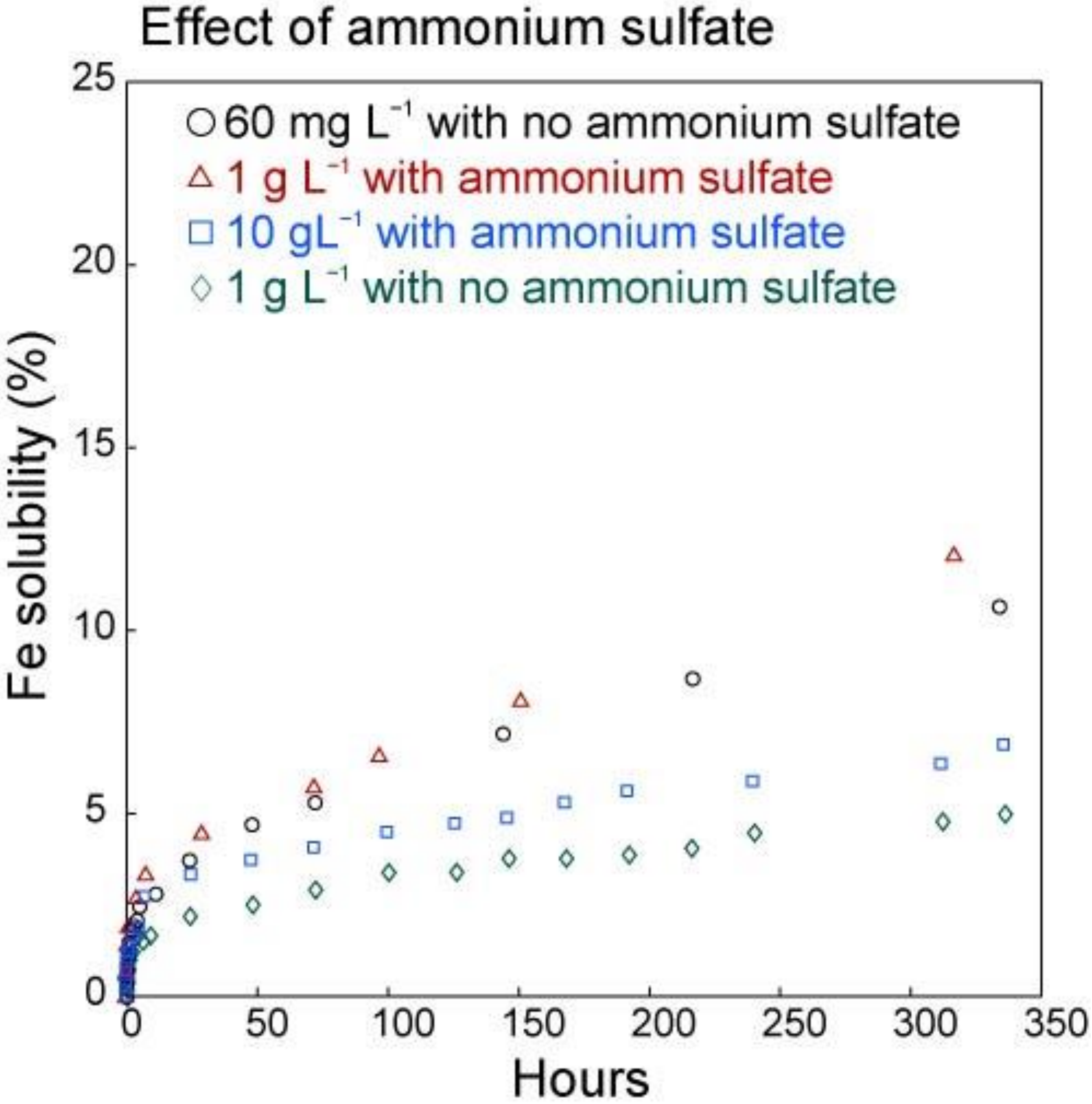

Fig. 1 Comparison of Fe solubility in solution (%) measured at two different dust/liquid ratios of 1 g L^{-1} (red triangles) and 10 g L^{-1} (blue squares) in 0.05 mol L^{-1} sulfuric acid solution with 1 mol L^{-1} $(NH_4)_2SO_4$ ($I = 3.15$ mol kg^{-1}), and dust/liquid ratios of 60 mg L^{-1} (black circles) and 1 g L^{-1} (green diamonds) in 0.005 mol L^{-1} sulfuric acid solution without $(NH_4)_2SO_4$ (pH = 2.0).

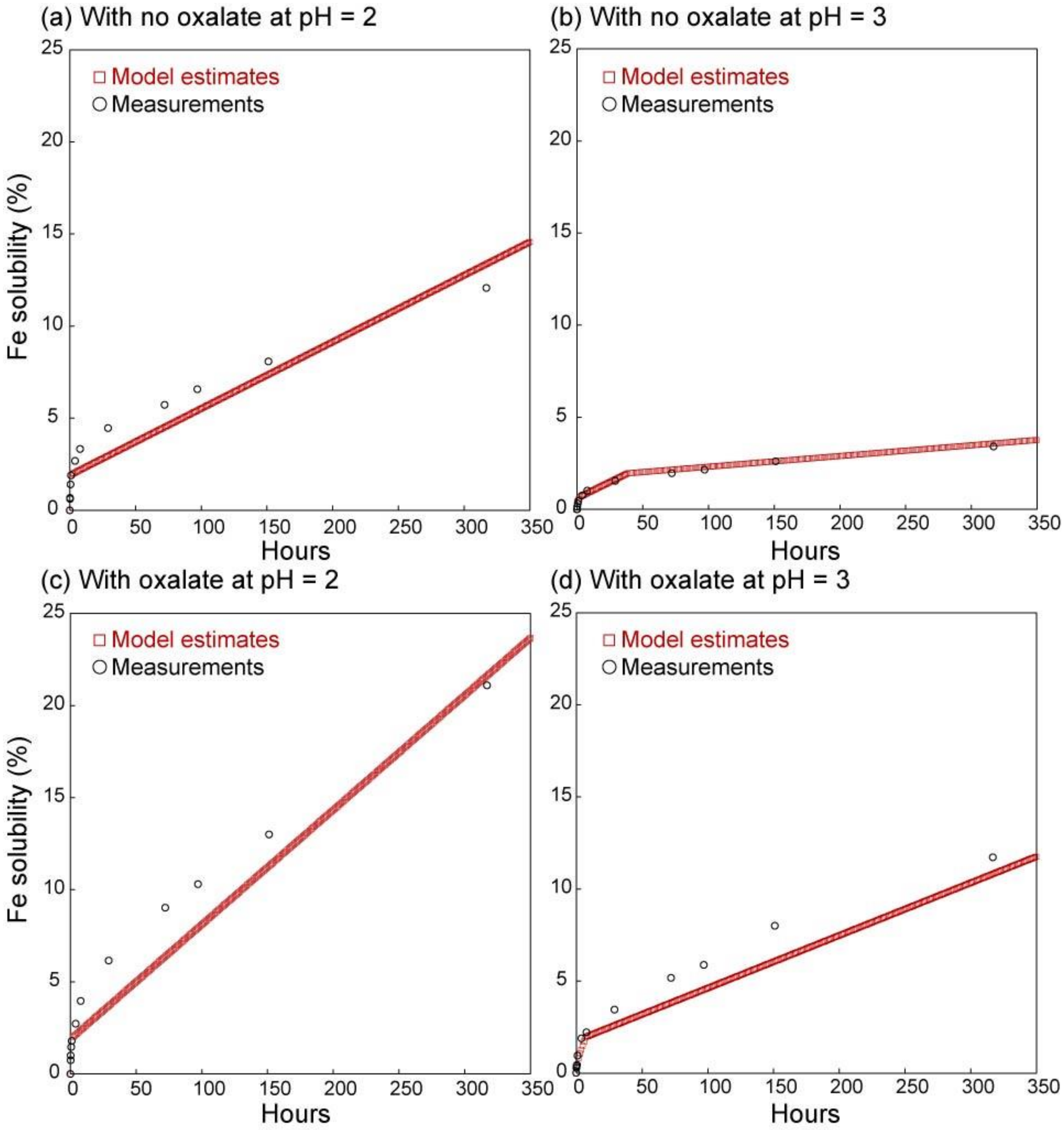

Fig. 2 Comparison of Fe solubility in solution (%) predicted using equation (1) with our measured Fe dissolution rates **(a)** with no oxalate at pH = 2, 0.05M H_2SO_4, 1M $(NH_4)_2SO_4$, **(b)** with no oxalate at pH = 3, 0.005M H_2SO_4, 1M $(NH_4)_2SO_4$, **(c)** with oxalate at pH = 2.1, 0.05M H_2SO_4, 1M $(NH_4)_2SO_4$, and 0.03 M $Na_2C_2O_4$, **(d)** with oxalate at pH = 3, 0.005M H_2SO_4, 1M $(NH_4)_2SO_4$, and 0.03 M $Na_2C_2O_4$. The red squares are calculated using equation (1) from the rate constants used in this study at each hour. The black circles are our measured data. The values of pH in solution are calculated using E-AIM (Wexler and Clegg, 2002, http://www.aim.env.uea.ac.uk/aim/aim.php).

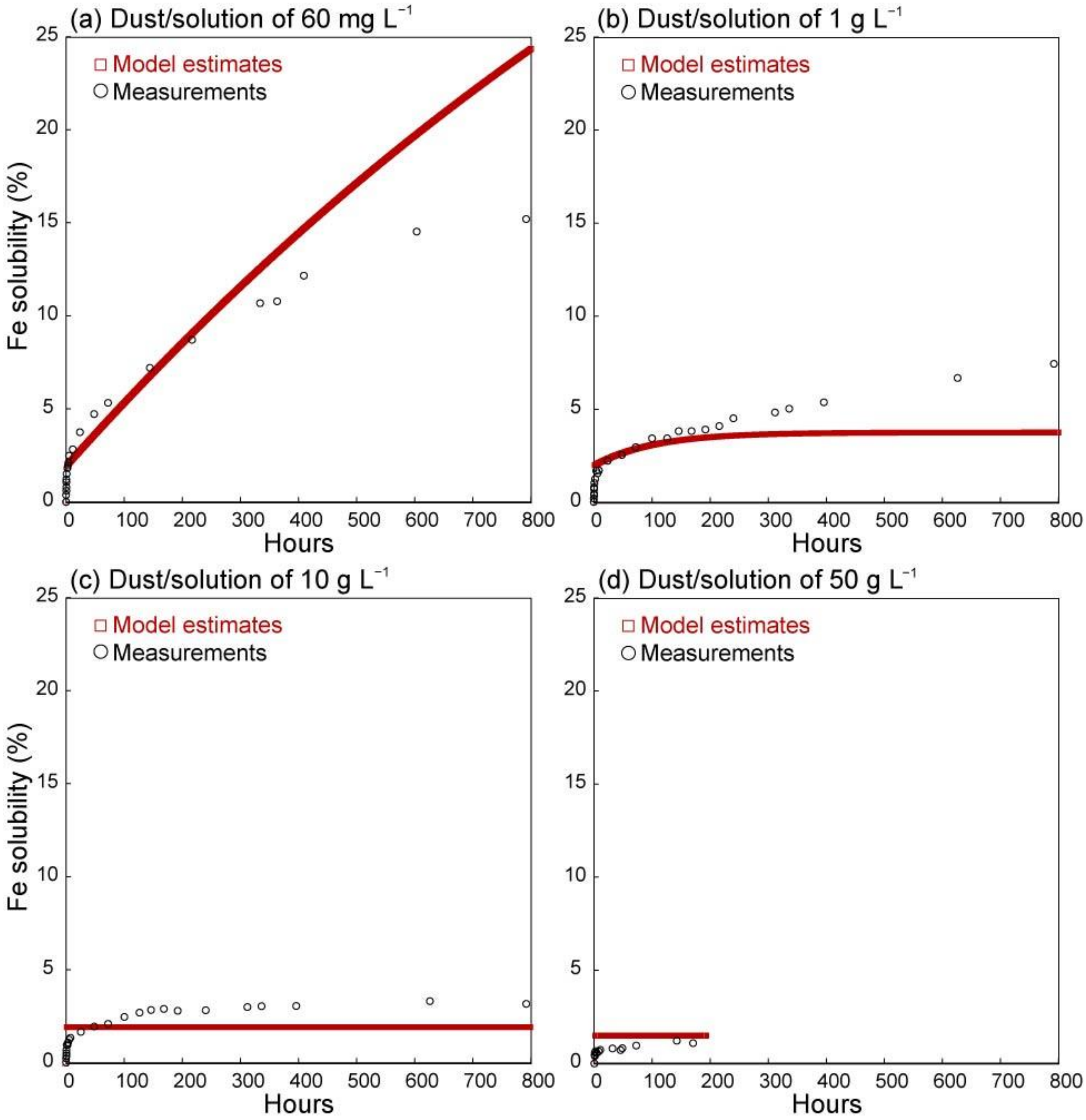

Fig. 3 Comparison of Fe solubility in solution (%) predicted using equation (1) with the measured Fe dissolution rates at pH = 2, 0.005M H_2SO_4, and dust/solution of **(a)** 60 mg L^{-1}, **(b)** 1 g L^{-1}, **(c)** 10 g L^{-1}, and **(d)** 50 g L^{-1}. The red squares are calculated using equation (1) from the equilibrium constant ($mol^2\ kg^{-2}$) used in this study at each hour. The black circles are our measured data. The fraction of total dissolved Fe present as Fe(III) is prescribed at pH = 2 (0.2) in this calculation to emulate the experimental conditions, while the photochemical redox cycling between Fe(III) and Fe(II) in solution is explicitly simulated in our global model (Lin et al., 2014). The large fraction of Fe(II) in solution under the dark conditions is likely associated with the Fe dissolution of Fe(II)-containing solids (Cwienty et al., 2008). The initial fraction of Fe speciation is not critical in estimating the Fe redox speciation in aerosol water, because Fe(II) is quickly oxidized to Fe(III) in oxygenated water (Deguillaume et al., 2010).

(a) Latitudinal variability of soluble Fe

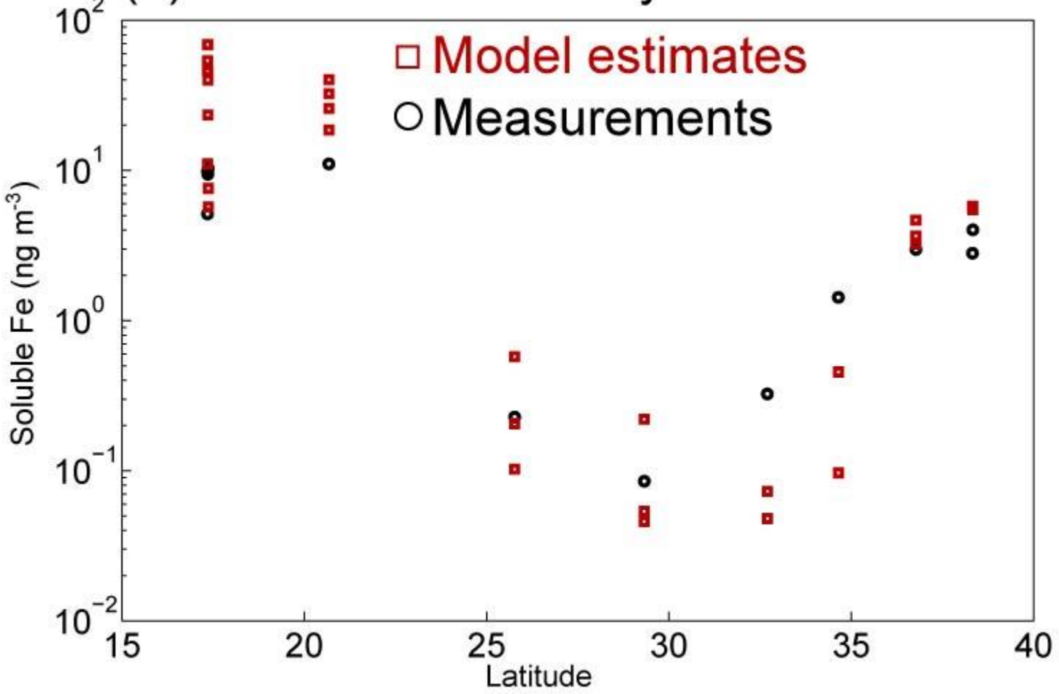

(b) Longitudinal variability of soluble Fe

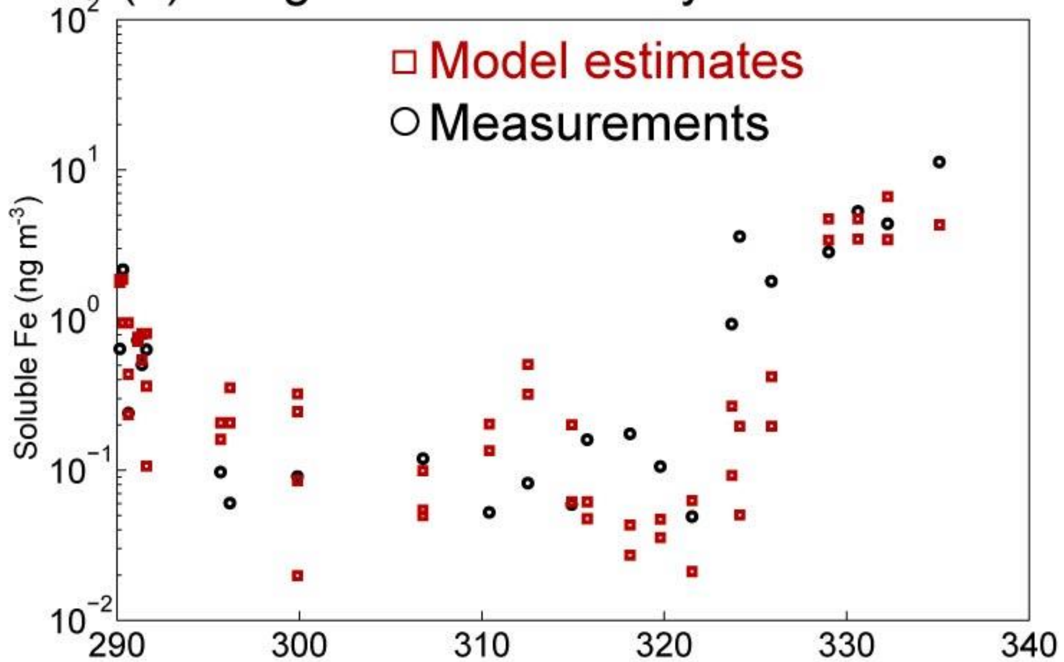

Fig. 4 Comparison of simulated (red squares) and observed (black circles) soluble Fe concentration (ng m^{-3}) during **(a)** 2010 and **(b)** 2011 U.S. GEOTRACES cruise over the North Atlantic (Wozniak et al., 2013, 2015). The number of modeled data points (84) is larger than the measurements (37), because each daily average is calculated for each sampling date at each center of cruise location.

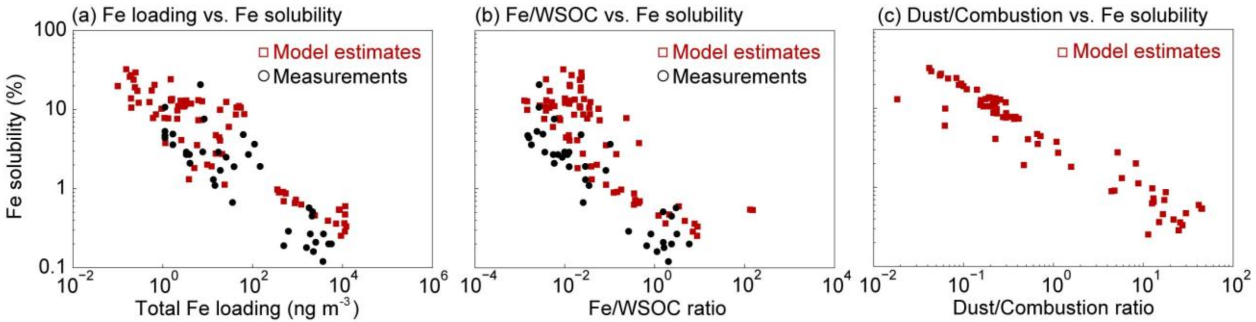

Fig. 5 **(a)** Atmospheric loading of total aerosol Fe (ng m^{-3}) versus Fe solubility for model estimates (red squares) and measurements (black circles) over the cruise tracks. **(b)** The Fe/WSOC molar ratio versus Fe solubility for model estimates (red squares) and measurements (black circles) over the cruise tracks. **(c)** The dust/combustion ratio for soluble Fe versus percent of soluble Fe in total Fe for model results over the cruise tracks. The measurements are obtained from Wozniak et al., (2013, 2015). The number of modeled data points (84) is larger than the measurements (37), because each daily average is calculated for each sampling date at each center of cruise location.

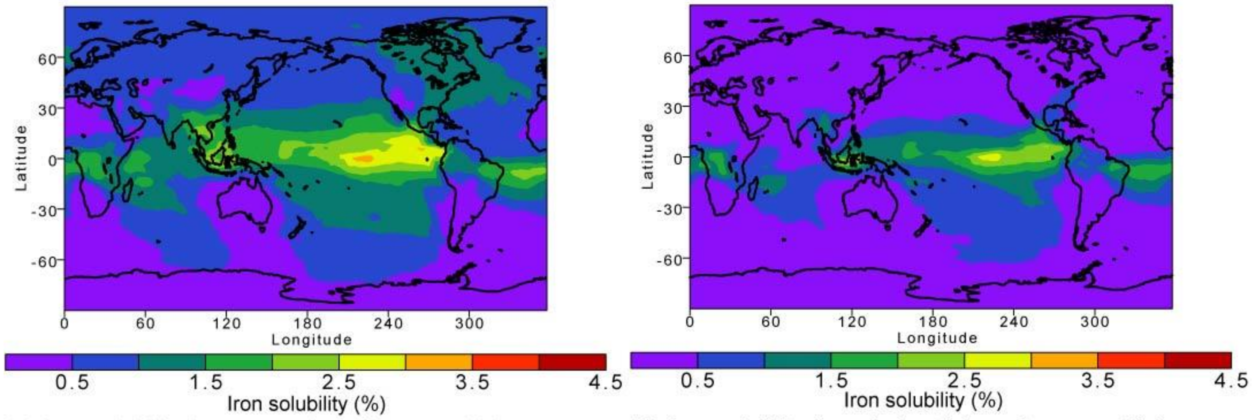
(a) Iron solubility in present days from base case

(b) Iron solubility in preindustrial era from base case

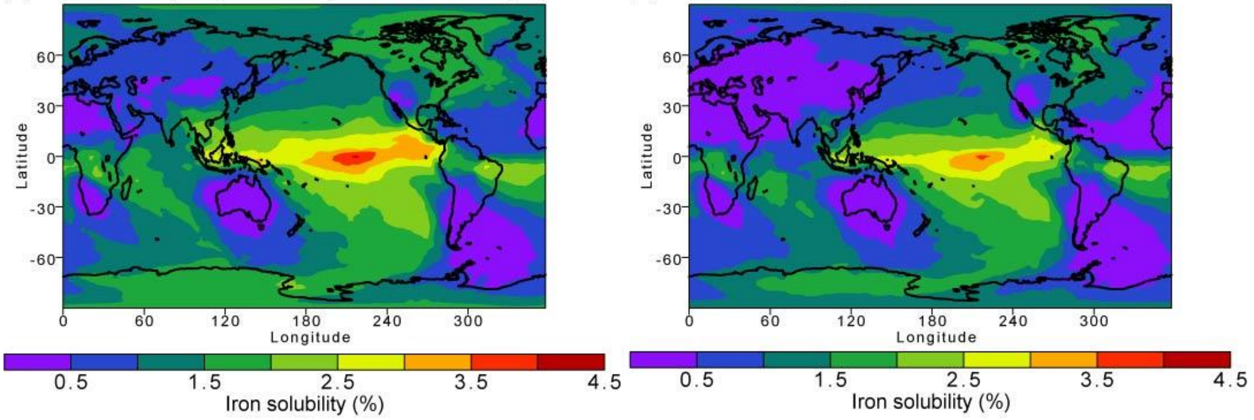
(c) Iron solubility in present days from sensitivity case

(d) Iron solubility in preindustrial era from sensitivity case

Fig. 6 Ratio (%) of the soluble to total Fe deposition for mineral dust in **(a)** present days from base simulations, **(b)** preindustrial era from base simulations, **(c)** present days from sensitivity simulations, and **(d)** preindustrial era from sensitivity simulations. The formation of the amorphous $Fe(OH)_3(s)$ suppresses the oxalate-promoted dissolution from mineral aerosols in the base simulations, while no such effect was considered for quasi-light-induced reductive dissolution in the sensitivity simulation (i.e., $f_3 = 1$).

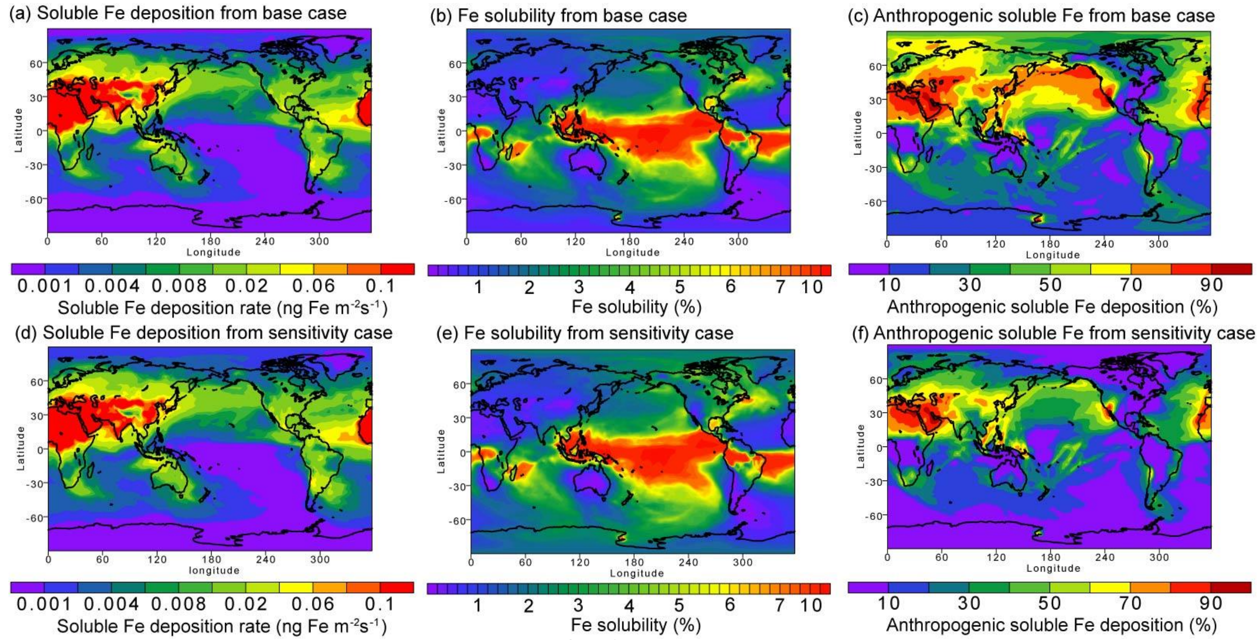

Fig. 7 Deposition of soluble Fe (ng Fe m^{-2} s^{-1}) from dust and combustion sources to the oceans in present days **(a)** from base simulations and **(d)** from sensitivity simulations, Fe solubility in present days **(b)** from base simulations and **(e)** from sensitivity simulations, and ratio of increase from preindustrial to present to soluble Fe deposition in present days **(c)** from base simulations and **(f)** from sensitivity simulations. The formation of the amorphous $Fe(OH)_3(s)$ suppresses the oxalate-promoted dissolution from mineral aerosols in the base simulations, while no such effect was considered for quasi-light-induced reductive dissolution in the sensitivity simulation (i.e., $f_3 = 1$).